



Phenomenological study on the production of $t \bar{t} Z'$ at the LHC in final states with taus

In partial fulfillment of the requirements for the Degree of
Physicist

Liliana Quintero Zambrano

Advisor professor
Andrés Flórez, Ph.D.

Universidad de los Andes
Faculty of science
Physics department

Bogotá D.C. Colombia
June 2021

Contents

1	Introduction	1
1.1	The Standard model	1
1.2	Objectives	3
2	Theoretical Framework	4
2.1	Why Quantum Field Theory	4
2.2	From classical mechanics to field theory	4
2.2.1	Lagrangian formalism	4
2.2.2	Euler-Lagrange equations	5
2.2.3	Hamiltonian formalism	7
2.2.3.1	Canonical quantization	8
2.3	The complex scalar field	8
2.3.1	Klein-Gordon equation	8
2.3.2	Fourier decomposition	9
2.3.3	Noether's theorem	10
2.3.3.1	Conserved quantities	10
2.3.4	Normal ordering	11
2.3.5	Propagators	12
2.4	Vector fields	13
2.5	Dirac Equation	14
2.5.1	Particle interpretation	14
2.5.2	Spin	15
2.5.3	Feynman propagator	16
2.6	Group theory	16
2.6.1	Lie Groups	17
2.6.1.1	Group Representation	17
2.7	QED	18
2.8	EWT	19
2.8.1	Weak interaction	19
2.8.2	The Higgs Mechanism	21
2.9	QCD	23
2.10	Interactions	24
2.10.1	The S matrix	25
2.10.2	Cross Sections and Feynman Amplitude	26
2.10.3	Feynman Rules	27

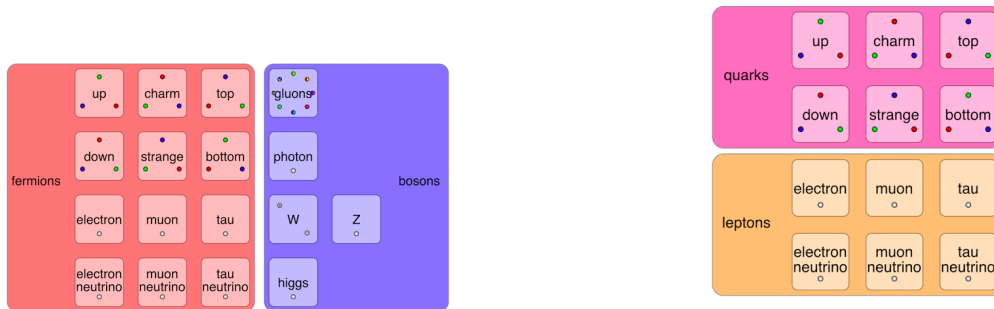
3	Beyond the Standard Model	30
3.1	Z' physics	30
3.2	Recent results regarding Z' production	33
4	Signal simulation and data analysis	35
4.1	Madgraph	35
4.2	MadAnalysis	37
4.3	MadAnalysis expert mode	37
5	Collider physics and experimental parameters	38
5.1	The Large Hadron Collider	38
5.1.1	Detectors	39
5.1.1.1	CMS	40
5.2	Experimental parameters: Kinematic and topological variables of the signal	42
5.2.1	Pseudorapidity and azimuthal angle	42
5.2.2	Transverse momentum	42
5.2.3	Angular distance	43
6	Phenomenological analysis	44
6.1	Preliminary analysis	44
6.2	Event classification	47
6.3	Selection criteria	48
6.3.1	Fully hadronic channel	48
6.3.2	Semi-leptonic channel	52
6.3.2.1	High mass classification	56
6.3.2.2	Low mass classification	58
6.4	Efficiencies	58
6.5	Significances	64
7	Conclusions	68
A	Covariant notation	69
B	Euler-Lagrange equations for fields	70
C	Hamiltonian formalism; Legendre transformation	71
D	Noether's theorem demonstration	72

1 Introduction

1.1 The Standard model

The standard model of particles (SM) is a theory based on the framework of quantum field theory (QFT) that achieves to accurately describe all known elementary particles, which are the ultimate constituents of matter at their smallest scale, and three of the four fundamental forces. The SM, in its most general point of view, consists of two dynamical theories: electroweak theory (EWT) and quantum chromodynamics (QCD). These theories explain phenomena involving fundamental particles and their interactions. The SM has successfully explained almost all experimental results and has precisely predicted a wide variety of phenomena [1].

The heart of QFT is that every particle and every wave in the universe is an excited state of a quantum field that permeates all space and time [2]. Particles are defined as an energy quantum associated to an excitation of a quantum field, which are uniquely described by their own particular quantum numbers. Particles are classified into two families: fermions, the fundamental building blocks of matter, and bosons, force carriers which mediate interactions. There are seventeen types of particles as shown in Figure (1a). For each particle there is an antiparticle, which has the same mass, lifetime and spin value as its corresponding particle but the spin-components and all the internal quantum numbers are opposite [1]. For example, the positron is the antiparticle of the electron, but there are cases in which the particle is its own antiparticle, as with photons [1].



(a) Fermions and Bosons classification of the SM. (b) Fermions classified into quarks and leptons where the columns represent generations one to three from left to right.

Figure 1: Diagrams of all the fundamental particles of the standard model classified ¹.

¹Image taken from: <http://physics.info/standard/>

Bosons are particles with integer spin that obey Bose-Einstein statistical rules [3] and are responsible of the interactions among particles. There are scalar bosons, such as the Higgs boson with spin 0, and vector bosons (gluons, photons, W^\pm and Z^0 bosons) with spin 1; where the former is described by a scalar field and the latter by vector fields.

On the other hand, fermions are particles that obey Fermi-Dirac statistics [4] and structure all the matter around us. Elementary fermions have spin 1/2 and can be classified into leptons and quarks, as shown in the Figure (1b). There are three groups of fermions, referred to as families. The known stable matter in the Universe is composed of the first family, which is the lightest in mass (u, d, e, ν_e). The other two families, (c, s, μ , ν_μ) and (t, b, τ , ν_τ), are heavier and decay to the first family. Quarks compose all the observed particles undergoing strong interactions i.e. hadrons (mesons and baryons). Quarks have color charge, which is another quantum number that arose to explain how these particles could coexist in the same quantum states without violating Pauli's exclusion principle [5]. Experimentally, quarks have been generally observed in bound states of two, three and up to five quarks, forming the so called non-fundamental hadronic states. This is an exclusive feature of quarks due to the nature of the strong interaction; leptons, on the other hand, do not behave this way and have been observed as "free" particles.

The SM describes the electromagnetic, the weak and the strong interactions. The mathematical framework used to describe the dynamical behavior of point-like charged particles, notably electrons, the electromagnetic field, and their interactions is called quantum electrodynamics (QED) [1]. The weak interaction explains the radiative decay processes of hadrons and leptons. This theory consists of a $SU(2)$ symmetry, in which our six leptons are classified into three left-handed doublets (e, ν_e), (μ, ν_μ), (τ, ν_τ) and the carriers that mediate interactions between these doublets are the W^\pm bosons for charged current interactions and the Z^0 boson for neutral current processes. From these two forces the electroweak theory (EWT) emerges: a $SU(2)_L \times U(1)_Y$ symmetry [1] (EXPLICAR L Y Y) that describes the phenomena involving fermions at high energies. The strong force, on the other hand, is described by the $SU(3)_C$ EXPLICAR C symmetry of QCD. The source of this force is the color charge, which all quarks carry. Eight gluons are the carriers of the strong interaction, which are associated to the number of generators of rotation in the $SU(3)_C$ symmetry group. QCD combined with EWT and the Higgs mechanism, this last being the process through which SM particles acquire mass, forms the complete framework of the SM.

Although the SM explains quite accurately all the phenomena and interactions at low energies, it also contains many parameters that are put in by hand from experimental measurements, such as the particle masses, the mixing angles and more. It is also incapable

of describing multiple experimental facts, such as the oscillation of neutrinos, the lightness of the Higgs boson, the existence of dark matter or the matter-antimatter asymmetry in the universe [6]. In addition, the SM is not valid at energies above the Planck scale (10^{19} GeV), where gravity cannot be ignored. Consequently, it is expected that interesting physics remains to be discovered as we move into energy levels beyond the energy scales explored in the SM, i.e. (~ 100 GeV) [7]. Some extensions of the SM include heavy gauge bosons called W' and Z' bosons, which correspond to heavier versions of the SM W and Z bosons. The experimental discovery of new heavy gauge bosons would have much greater implications than just the existence of a new vector boson, as it would be an indicator of new physics and a cornerstone to the development of new theories that could explain the problems encountered in the SM.

1.2 Objectives

The main purpose of this thesis is to perform a phenomenological study on the production of Z' bosons through a top-antitop fusion process ($t \bar{t} Z'$), considering semi-leptonic final states of the top pair system and hadronic tau pairs from the Z' boson. This is accomplished by performing simulations on the production of the $t \bar{t} Z'$ processes at The Large Hadron Collider (LHC), considering different couplings to light and heavy fermions and different Z' masses, using an effective field theory approach. The dependence of the production cross section as function of mass, for different coupling scenarios, together with some kinematic and topological variables are also studied.

In order to study and distinguish the Z' production simulations of the signal and possible background processes, including the LHC experimental conditions, are generated using various software packages, explained in detail in Section 4. Finally, using all the analysed data, a preliminary phenomenological analysis will be performed to determine the feasibility of implementing an analysis at the CMS experiment.

2 Theoretical Framework

2.1 Why Quantum Field Theory

The SM embodies a wide variety of mathematical concepts that accurately outlines the theoretical description and concepts of most of the phenomena we observe in nature. Given that in the quantum world, particles generally move at high speeds, in multiple cases close to the speed of light, a relativistic theory of quantum mechanics had to be developed, giving rise to QFT. This is the framework under the SM is built upon. In QFT, particles are associated with fundamental fields, that are functions of space-time coordinates. But why is it necessary to work with fields? The search of a field theory seems quite natural when one considers that the most accurate and complete classical theory of phenomena is, in fact, a field theory: Maxwell's electromagnetism.

One can think of QFT as an extension on QM as it, in a certain way, extends particles to the concept of fields. This transition was necessary in order to describe the behavior of particles and interactions as QM itself presents some limitations. For starters, it does not involve processes of creation or annihilation of particles such as the β -decay, therefore, these processes can only be handled by going over QFT. Another problem of particle quantum mechanics is that it is developed by definition only in the non-relativistic limit, which represents a narrow scope of reality. Furthermore, space and time are treated differently in QM, which presents a problem when treating with relativistic phenomena, which is observed in nature [8].

Since the development of QFT, it is clear that fields are necessary to describe particle interactions. A field is typically either a scalar, vector, tensor, or spinor field, that has a well-defined value at every point in space and time. When working with fields the covariant notation will be used (a brief explanation of covariant notation is presented in Appendix A).

2.2 From classical mechanics to field theory

2.2.1 Lagrangian formalism

The Lagrangian formalism allows the study and description of all excitations and interactions in a physical theory. This formalism emerges from classical physics and its concept and generalizations were first formulated by Joseph-Louis Lagrange in late 18th century

and this formulation is a cornerstone of modern and classical physics. A Lagrangian is a function of the coordinates of a system from which we can obtain its evolution, its conserved quantities and study its properties at any point in space-time. For particles moving under a conservative force, the non-relativistic Lagrangian corresponds to the difference of the kinetic and potential energies:

$$L = K - U. \quad (2.1)$$

From this definition other important concepts emerge, the Lagrangian density, defined as $L = \int d^3x \mathcal{L}$, so that the integration of the Lagrangian density over the spatial variables gives the Lagrangian function and the Action, which was introduced in order to solve dynamical problems, defined by William Hamilton in 1834 as

$$\mathcal{A} = \int_{t_1}^{t_2} dt L(q_r(t), \dot{q}_r(t), t). \quad (2.2)$$

The Lagrangian depends explicitly on time if there is a source or sink of energy in the system. Given this Action functional, it is possible to determine the corresponding equations of motion of the particle i.e. it is possible to determine the path that a given particle will take. This path can be determined by applying the Hamilton's principle or the principle of least action, which dictates that the evolution of a physical system is such that the action \mathcal{A} remains stationary as the system evolves [9]. The concept of stationary in case of integrals, refers to the concept that 'the integral along the given path has the same value to within first order infinitesimals as that along all neighboring paths' [9] i.e. it vanishes at first order derivation and so the variation of the lineal integral defined in Equation (2.2) must be zero:

$$\delta \mathcal{A} = \delta \int_{t_1}^{t_2} dt L(q_r(t), \dot{q}_r(t), t) = 0, \quad (2.3)$$

where $r = 1, \dots, n$ and these q_r correspond to the generalized coordinates that describe the configuration of the system and correspond to a particular point in a cartesian hyper-space (the configuration space) where the q 's form the n coordinate axes [9].

2.2.2 Euler-Lagrange equations

One implication of the principle of least action is that it leads to the equation of motion of the system, considering small perturbations of the coordinates one gets:

$$\delta L = \frac{\partial L}{\partial q_r} \delta q_r + \frac{\partial L}{\partial \dot{q}_r} \delta \dot{q}_r. \quad (2.4)$$

which can be coupled into Equation (2.3) so that the integral becomes

$$\delta \mathcal{A} = 0 = \int_{t_1}^{t_2} dt \left[\frac{\partial L}{\partial q_r} \delta q_r + \frac{\partial L}{\partial \dot{q}_r} \delta \dot{q}_r \right], \quad (2.5)$$

and by integrating by parts the second term in order to simplify this equation, one obtains

$$\int_{t_1}^{t_2} dt \frac{\partial L}{\partial \dot{q}_r} \delta \dot{q}_r = \frac{\partial L}{\partial \dot{q}_r} \delta q_r \Big|_{t_1}^{t_2} - \int_{t_1}^{t_2} dt \frac{d}{dt} \left(\frac{\partial L}{\partial \dot{q}_r} \right) \delta q_r = - \int_{t_1}^{t_2} dt \frac{d}{dt} \left(\frac{\partial L}{\partial \dot{q}_r} \right) \delta q_r. \quad (2.6)$$

In Equation 2.6, the first term of the second equality is zero due to the boundary conditions on δq_r , as it represents an infinitesimal variation of the path, the end points (t_1, t_2) shall not vary. Replacing this obtained result in Equation (2.5)

$$\int_{t_1}^{t_2} dt \left[\frac{\partial L}{\partial q_r} - \frac{d}{dt} \left(\frac{\partial L}{\partial \dot{q}_r} \right) \right] \delta q_r = 0. \quad (2.7)$$

Since taking $\delta q_r = 0$ is a trivial solution, $\delta \mathcal{A} = 0$ implies

$$\frac{\partial L}{\partial q_r} - \frac{d}{dt} \left(\frac{\partial L}{\partial \dot{q}_r} \right) = 0 \quad \rightarrow \quad \frac{\partial L}{\partial q_r} = \frac{d}{dt} \left(\frac{\partial L}{\partial \dot{q}_r} \right). \quad (2.8)$$

This last expression is known as the Euler-Lagrange equations which correspond to the equations of motion of the system.

When working with fundamental particles it is necessary to go over the field theory and consequently systems will now be a field $\phi(x)$ or a set of fields $\phi^A(x)$, and the Action will now become

$$\mathcal{A} = \int_{\Omega} d^4x \mathcal{L} \left(\phi^A(x), \partial_{\mu} \phi^A(x) \right), \quad (2.9)$$

where using the definition of the Lagrangian density \mathcal{L} allowed us to put time and space in the same level in the integration.

From this definition of the Action, now in terms of the fields and its derivatives, the equations of motion can be obtained via the principle of least action and the Euler-Lagrange equations become:

$$\partial_{\mu} \left(\frac{\partial \mathcal{L}}{\partial (\partial_{\mu} \phi^A)} \right) = \frac{\partial \mathcal{L}}{\partial \phi^A}. \quad (2.10)$$

The derivation of these equations is made in Appendix B.

2.2.3 Hamiltonian formalism

Although the Lagrangian formulation can accurately describe the system, another alternative method is to work in the Hamiltonian formulation, which offers a useful framework for theoretical extensions in many areas of physics such as statistical or quantum mechanics. With this new formulation it is desirable to describe the motion in terms of first-order equations of motion in contrast of the Lagrangian formulation, which involves a second-order equation. For this, the generalized momentum (conjugate to q_r) is introduced as

$$p_r = \frac{\partial L(q_r, \dot{q}_r)}{\partial \dot{q}_r}. \quad (2.11)$$

The idea behind this new formulation is to perform a change of variables from (q_r, \dot{q}_r, t) to (q_r, p_r, t) through a Legendre transformation (for the complete derivation see Appendix C). Then the Hamiltonian is defined as

$$H(p, q) = p_r \dot{q}_r - L(q, \dot{q}_r), \quad (2.12)$$

which has the differential

$$dH = p_r d\dot{q}_r + \dot{q}_r dp_r - \left(\frac{\partial L}{\partial q_r} dq_r + \frac{\partial L}{\partial \dot{q}_r} d\dot{q}_r \right) = \dot{q}_r dp_r - \dot{p}_r dq_r. \quad (2.13)$$

The last equality is obtained by using Equation (2.11) and Equation (2.8). Since dH can also be written as

$$dH = \frac{\partial H}{\partial q_r} dq_r + \frac{\partial H}{\partial p_r} dp_r, \quad (2.14)$$

the following relations, known as Hamilton's equations of motion, are obtained:

$$\dot{p}_r = -\frac{\partial H}{\partial q_r}, \quad \dot{q}_r = \frac{\partial H}{\partial p_r}. \quad (2.15)$$

Going over field theory is a straight forward process, taking the momenta canonical to the fields ϕ^A to be

$$\Pi_A = \frac{\partial \mathcal{L}}{\partial \dot{\phi}^A}, \quad (2.16)$$

in analogy with Equation (2.11). From this, the Hamiltonian becomes:

$$\mathcal{H} = \Pi_A \dot{\phi}^A - \mathcal{L}, \quad (2.17)$$

where \mathcal{H} is the hamiltonian density, i.e

$$H = \int d^3x \mathcal{H}, \quad (2.18)$$

2.2.3.1 Canonical quantization

The canonical quantization is a procedure that allows to take canonically conjugate variables and transform them into operators, thereby its a way to go from the Hamiltonian formalism of classical dynamics to a quantum theory. The Poisson bracket of classical mechanics is defined as:

$$\{f, g\} = \frac{\partial f}{\partial q_r} \frac{\partial g}{\partial p_r} - \frac{\partial f}{\partial p_r} \frac{\partial g}{\partial q_r}. \quad (2.19)$$

Therefore, the Poisson bracket of the canonical variables is

$$\{q_r, p_s\} = \delta_{rs}, \quad (2.20)$$

which through the quantization morphs into the structure of commutation relations between operators, so that

$$[q_r, p_s] = i\delta_{rs} \rightarrow [\phi(\mathbf{x}), \Pi(\mathbf{y})] = i\delta^3(\mathbf{x} - \mathbf{y}). \quad (2.21)$$

This last step helps us setting footage on the field theory.

2.3 The complex scalar field

The simplest field that could be considered is the scalar field, for which there is a single number associated with every point in space-time [10]. These fields have orbital angular momentum and spin of zero, and are invariant under Lorentz transformations. In the SM, until now, there is only one scalar field associated to a fundamental particle, the Higgs Boson. Due to their simplicity, scalar fields provide a great starting point to study field theory.

2.3.1 Klein-Gordon equation

For free particles of rest mass m , energy and momentum are related by:

$$E^2 = \mathbf{p}^2 + m^2, \quad (2.22)$$

which in covariant notation and can written as

$$p^\mu p_\mu - m^2 = 0. \quad (2.23)$$

Treating the 4-momentum as an operator in the space representation, we get that acting on a wavefunction $p_\mu \rightarrow i\partial_\mu \equiv i\partial/\partial x^\mu$. Therefore, when acting Equation (2.23) on a scalar field $\phi(x)$ we obtain the Klein-Gordon equation

$$(\square + m^2) \phi(x) = 0, \quad (2.24)$$

where $\square = \partial_\mu \partial^\mu$.

This equation is covariant and was the first equation capable of describing quantum theory in the relativistic limit. Schrödinger's equation could describe all phenomena in atomic physics but it was not invariant under Lorentz transformations. The Klein-Gordon equation works successfully in the relativistic theory due to the fact that space and time are treated equally. Nevertheless, when solving this equation one finds solutions that involve energies that can be negative and arbitrarily large (not bounded), thus the system will not have a ground state. The negative solutions are associated with negative probability and this second problem was beyond anything that could be accepted as a reasonable option at the time. As will be presented in Section 2.3.3.1 the problem of the negative values of the energy was later discovered to represent antiparticles.

2.3.2 Fourier decomposition

If one considers a scalar field, the simplest Lagrangian that is Lorentz invariant is precisely the one associated with the Klein-Gordon Equation (2.24). For a complex scalar field it is

$$\mathcal{L} = (\partial^\mu \phi^\dagger)(\partial_\mu \phi) - m^2 \phi^\dagger \phi. \quad (2.25)$$

Treating ϕ and ϕ^\dagger as independent fields and following the equations of motion (B.8), it is obtained:

$$(\square + m^2) \phi(x) = 0, \quad (2.26)$$

$$(\square + m^2) \phi^\dagger(x) = 0. \quad (2.27)$$

Because the Klein-Gordon equation is a homogeneous, linear differential equation, we can express its solutions as a linear superposition of plane waves [11].

$$\phi(x) \sim e^{\pm i p \cdot x} \quad \text{where,} \quad (2.28)$$

$$-i p \cdot x = i(\mathbf{p} \cdot \mathbf{x} - E_{\mathbf{p}} t). \quad (2.29)$$

In classical mechanics, the negative energy solutions can be dismissed as being unphysical. However, in quantum mechanics all solutions are required to form a complete set of states, and the negative energy solutions simply cannot be discarded [12]. In fact, the most general solution is obtained if we make a Fourier expansion of our fields $\phi(x)$ and $\phi^\dagger(x)$, such that they can be written in term of creation $a^\dagger(\mathbf{p})$ and annihilation $a(\mathbf{p})$ operators:

$$\phi(x) = \int \frac{d^3 p}{\sqrt{(2\pi)^3 2E_{\mathbf{p}}}} \left(a(\mathbf{p}) e^{-i p x} + \hat{a}^\dagger(\mathbf{p}) e^{i p x} \right), \quad (2.30)$$

$$\phi^\dagger(x) = \int \frac{d^3 p}{\sqrt{(2\pi)^3 2E_{\mathbf{p}}}} \left(\hat{a}(\mathbf{p}) e^{-i p x} + a^\dagger(\mathbf{p}) e^{i p x} \right). \quad (2.31)$$

It is also convenient to work in the Fourier space as plane waves are energy and momentum eigenfunctions and linear operations, including time and space derivatives, are simpler to perform and interpret physically [11].

2.3.3 Noether's theorem

To gain more inside on the theory it is necessary to consider that in any system there are invariances regarding some transformations and subsequently conserved quantities. Noether's theorem states that there's a conserved quantity associated with each continuous symmetry. A symmetry is a transformation that leaves the system invariant and it gives rise to conservation laws. For example, symmetries in time translation lead to conservation of energy, symmetries in spatial translations lead to conservation of linear momentum, and symmetries in rotations lead to conservation of angular momentum [11] [8]

In other words Noether's theorem states that, if after a transformation our Lagrangian changes by an addition of a 4-divergence ($\delta \mathcal{L} = \partial_\mu W^\mu$ for any W^μ) that implies the existence of a conserved current, i.e. $\partial_\mu J^\mu = 0$, where J^μ is the Noether current [2]. The complete derivation of Noether's theorem is presented in Appendix D.

2.3.3.1 Conserved quantities

Because of the presence of a conserved current, the concept of a conserved charge, called the Noether charge, emerges as well. This conserved charge arises as a consequence of

performing the integral of the 0th component of the current J^μ , defining

$$Q \equiv \int d^3x J^0. \quad (2.32)$$

and performing a time derivative

$$\frac{dQ}{dt} = \int d^3x \partial_0 J^0 = - \int d^3x \nabla \cdot \mathbf{J} = - \int_S d\sigma \cdot \mathbf{J} = 0 \quad (2.33)$$

the fourth equality is obtained using Gauss's theorem to change the volume integral to a surface integral, and the last equality follows from the boundary condition that the fields vanish at infinity [1]. And thus, the Noether charge corresponds to a conserved quantity.

The Lagrangian of Equation (2.25) is invariant under transformations of the form

$$\phi \rightarrow \phi' = e^{-iq\theta} \phi, \quad \phi^\dagger \rightarrow \phi'^\dagger = e^{iq\theta} \phi^\dagger, \quad (2.34)$$

where θ is independent of space-time. If θ is an infinitesimal parameter, then the variation of the field is expressed as $\delta\phi = -iq\theta\phi$ and $\delta\phi^\dagger = iq\theta\phi^\dagger$. As the Lagrangian is invariant under the transformations of Equation (2.34) then $\delta\mathcal{L} = 0$ and the conserved current is

$$J^\mu = iq \left[(\partial^\mu \phi) \phi^\dagger - (\partial^\mu \phi^\dagger) \phi \right], \quad (2.35)$$

Therefore, using Equations (2.30), (2.31) and (2.32):

$$Q = q \int d^3p \left[a^\dagger(\mathbf{p}) a(\mathbf{p}) - \hat{a}^\dagger(\mathbf{p}) \hat{a}(\mathbf{p}) \right] = q (N_a - N_{\hat{a}}). \quad (2.36)$$

Being N_a and $N_{\hat{a}}$ the number operators for the quanta created with momentum \mathbf{p} . With this, one can see that N_a corresponds to the number of particles and has a positive contribution to the charge Q , and $N_{\hat{a}}$ to the number of antiparticles which add the same "amount" of charge but with opposite sign. This also tells us that the total charge in particles and antiparticles is conserved as a consequence of Noether's theorem [8].

2.3.4 Normal ordering

From the Lagrangian in Equation (2.25) and the definitions of the canonical momenta (Equation (2.16))

$$\Pi(x) = \dot{\phi}^\dagger(x), \quad \Pi^\dagger(x) = \dot{\phi}(x), \quad (2.37)$$

and then the total Hamiltonian associated with the complex scalar field Lagrangian

(Equation (2.25)) is

$$H = \int d^3x \mathcal{H} = \int d^3x \left(\Pi^\dagger \Pi + \nabla \phi^\dagger \cdot \nabla \phi + m^2 \phi^\dagger \phi \right), \quad (2.38)$$

or explicitly, one can replace each term with the definition of ϕ and ϕ^\dagger given in Equations (2.30) and (2.31). But as mentioned in Section 2.3.1, there is a ground state problem with the system, thus the normal ordering (the normal ordering of X is denoted $:X:$) is introduced in the Hamiltonian of the system, this implies that whenever we encounter a product of creation and annihilation operators, we move all annihilation operators to the right of all creation operators as if the commutators were zero [8], so that we don't encounter negative infinite energies on the system. With this prescription the Hamiltonian of the system becomes

$$:H:= \int d^3p E_{\mathbf{p}} \left(a^\dagger(\mathbf{p}) a(\mathbf{p}) + \hat{a}^\dagger(\mathbf{p}) \hat{a}(\mathbf{p}) \right); \quad (2.39)$$

so that

$$\langle 0 | :H: | 0 \rangle = 0 \quad (2.40)$$

2.3.5 Propagators

To take into account interactions, it is included in the free particle Lagrangian formulation a source such that now the field obeys an in-homogeneous differential equation. In order to solve this equation a propagator, or Green function, is introduced:

$$\Delta F(p) = \frac{1}{p^2 - m^2 + i\epsilon}, \quad (2.41)$$

taking its Fourier transformation:

$$\begin{aligned} i\Delta F(x - x') &= \int \frac{d^3p}{(2\pi)^3 2E_{\mathbf{p}}} \left[\Theta(t - t') e^{-ip(x-x')} + \Theta(t' - t) e^{ip(x-x')} \right] \\ &= \left\langle 0 \left| \mathcal{T} \left[\phi(x) \phi^\dagger(x') \right] \right| 0 \right\rangle, \end{aligned} \quad (2.42)$$

where Θ is a step function and $\mathcal{T}[\dots]$ corresponds to the time-ordered product, which means that the operator with the later time must be put to the left of the operator with the earlier time [8], the complete propagator derivation is shown in Appendix ??.

2.4 Vector fields

As discussed earlier, there is another type of bosons which are called vector bosons. Vector bosons have integer spin of one and are the carriers of interactions included in the SM.

As seen in Section 2.3 the complex scalar field described particles with spin $s = 0$, for particles with integer but non zero spin we study more complex fields. For $s = 1$ a field $A^\mu(x)$ is considered and thereby a 4-vector A^μ is associated with every point in space-time of the field, where A^μ lives in the Minkowski space and therefore, transforms as a 4-vector under Lorentz transformations [2]. For vector fields, the corresponding Lagrangian is defined as:

$$\mathcal{L} = -\frac{1}{4}F_{\mu\nu}F^{\mu\nu} + \frac{1}{2}m^2 A_\mu A^\mu, \quad (2.43)$$

in which $F_{\mu\nu} = \partial_\mu A_\nu - \partial_\nu A_\mu$. To find the equations of motion for the vector field in this theory, the Euler-Lagrange Equations (B.8) are used and we get that

$$\partial_\mu(\partial^\mu A^\nu - \partial^\nu A^\mu) + m^2 A^\nu = 0, \quad (2.44)$$

which can also be written as

$$(\square + m^2)A^\nu = 0. \quad (2.45)$$

This equation is known as the Proca equation, it is similar to the Klein Gordon Equation (2.24) and thus the plain wave solutions are very similar. In this case the quantized expression for A^μ in terms of creation and annihilation operators is

$$A^\mu(x) = \int \frac{d^3p}{\sqrt{(2\pi)^3 2E_{\mathbf{p}}}} \sum_{\lambda=1}^3 \left(\epsilon_\lambda^\mu(\mathbf{p}) a_\lambda(\mathbf{p}) e^{-ipx} + \epsilon_\lambda^{\mu\dagger}(\mathbf{p}) \hat{a}_\lambda^\dagger(\mathbf{p}) e^{ipx} \right), \quad (2.46)$$

where $\lambda = \{1, 2, 3\}$ denotes the three independent polarization degrees of freedom of the Polarization 4-vector $\epsilon^\mu(\mathbf{p})$ [2]. In the same way as we encountered in scalar fields one finds the normal ordered hamiltonian to be

$$:H:= \int d^3p E_{\mathbf{p}} \sum_{\lambda=1}^3 \left(a_\lambda^\dagger(\mathbf{p}) a_\lambda(\mathbf{p}) + \hat{a}_\lambda^\dagger(\mathbf{p}) \hat{a}_\lambda(\mathbf{p}) \right), \quad (2.47)$$

meaning that the total energy is the energy of all particles (and antiparticles) in all polarizations [2].

2.5 Dirac Equation

Although the Klein-Gordon equation led to a successful formalism it only describes integer spin particles. In order to consider systems of particles which satisfy the Pauli exclusion principle [5], i.e. obey Fermi-Dirac Statistics and have half-integer spin, it is necessary to go over the spinor fields [13].

Historically, the equation of motion for fermions was derived by 'accident' by Paul Dirac, when trying to solve the problem of negative energies and probabilities encountered in the Klein-Gordon equation. Dirac tried an alternative solution to solve this problem by proposing an equation that was linear in the time derivative and that represented the square root of Equation (2.22)[8]. The hamiltonian proposed by Dirac was:

$$H = \gamma^0(\boldsymbol{\gamma} \cdot \mathbf{p} + m), \quad (2.48)$$

where the γ^μ are 4x4 hermitian matrices such that, $\{\gamma^\mu, \gamma^\nu\} = 2g^{\mu\nu}$, $Tr(\gamma^\mu) = 0$ and $(\gamma^\mu)^\dagger = \gamma^0 \gamma^\mu \gamma^0$. Therefore, the Dirac Hamiltonian is a 4x4 matrix of operators that must act on a four-component state vector (spinor field), known as Dirac Spinors ψ . The conventional choice for the explicit form of the γ matrices is the Dirac-Pauli representation [12], such that:

$$\gamma^0 = \begin{pmatrix} I & 0 \\ 0 & -I \end{pmatrix} \quad \text{and} \quad \gamma^\mu = \begin{pmatrix} 0 & \sigma_k \\ -\sigma_k & 0 \end{pmatrix}, \quad (2.49)$$

where σ_k are the Pauli matrices.

2.5.1 Particle interpretation

The equation of motion also known as Dirac equation, that corresponds to the Hamiltonian in equation (2.48), is:

$$(i\rlap{\not{D}} - m)\psi(x) = 0, \quad (2.50)$$

where $\rlap{\not{D}} = \gamma^\mu \partial_\mu$. The explicit forms of the Dirac spinor field are expressed in terms of plane waves:

$$\psi(x) = \begin{cases} u(\mathbf{p})e^{-ip \cdot x} \\ v(\mathbf{p})e^{ip \cdot x}, \end{cases} \quad (2.51)$$

where $u(\mathbf{p})$ and $v(\mathbf{p})$ are doublets with components u_1, u_2 and v_1, v_2 , respectively. This four solutions correspond to those in which the energy that appears in the spinor is the positive physical energy of the particle/antiparticle. This result comes from following

the Feynman-Stückelberg interpretation, where "negative" solutions correspond to a new set of particles, that following explicitly the mathematical expressions would propagate "backwards" in time [12]. Nevertheless, the physical interpretation, referred these new set of particles as the associated antiparticle (anti-matter). Therefore, these antiparticles actually have positive energy and move forward in time, but are "mirror" states of the known SM particles, only different with charges and/or spins.

With the Fourier descomposition of the field, the $\psi(x)$ Dirac spinor correspond to:

$$\psi(x) = \int \frac{d^3p}{\sqrt{(2\pi)^3 2E_{\mathbf{p}}}} \sum_{s=1,2} \left(f_s(\mathbf{p}) u_s(\mathbf{p}) e^{-ipx} + \hat{f}_s^\dagger(\mathbf{p}) v_s(\mathbf{p}) e^{ipx} \right), \quad (2.52)$$

$$\bar{\psi}(x) = \int \frac{d^3p}{\sqrt{(2\pi)^3 2E_{\mathbf{p}}}} \sum_{s=1,2} \left(f_s^\dagger(\mathbf{p}) \bar{u}_s(\mathbf{p}) e^{ipx} + \hat{f}_s(\mathbf{p}) \bar{v}_s(\mathbf{p}) e^{-ipx} \right), \quad (2.53)$$

where $f_s(p)$, $f_s^\dagger(p)$, $\hat{f}_s(p)$, $\hat{f}_s^\dagger(p)$ are anihilation and creation operators for particles and antiparticles respectively, that follow anticommutation relations.

Following the same procedure of Sections 2.3.4 and 2.3.3.1 the total Hamiltonian and the corresponding Noether charge can be expressed as:

$$:H:= \int d^3p E_{\mathbf{p}} \sum_{s=1,2} \left(f_s^\dagger(\mathbf{p}) f_s(\mathbf{p}) + \hat{f}_s^\dagger(\mathbf{p}) \hat{f}_s(\mathbf{p}) \right), \quad (2.54)$$

$$:Q:= q \int d^3p \sum_{s=1,2} \left(f_s^\dagger(\mathbf{p}) f_s(\mathbf{p}) - \hat{f}_s^\dagger(\mathbf{p}) \hat{f}_s(\mathbf{p}) \right). \quad (2.55)$$

For this Hamiltonian, as stated earlier, it is guarantied that the creation and annihilation operators follow anticommutation relations and consequently, that it is not possible to create two particles or two antiparticles with the same spin and momentum, which is consistent with the Fermi-Dirac statistics.

2.5.2 Spin

Another remarkable feature to note about the theory is that as the Dirac Equation (2.50) must be relativistically covariant when preforming a Lorentz transformation, as a consequence, the angular momentum operator is found to be:

$$J_{\mu\nu} = i(x_\mu \partial_\nu - x_\nu \partial_\mu) + \frac{1}{2} \sigma_{\mu\nu}. \quad (2.56)$$

This shows how the spin arises naturally as the first term is the expression for the orbital angular momentum, and the second term is an "intrinsic" angular momentum [8].

The usual orbital angular momentum operator L does not commute with the Hamiltonian of the Dirac equation and neither does the spin operator $\frac{1}{2}\sigma_{\mu\mu}$, but the sum of these two, i.e the operator $J_{\mu\nu}$, referred to as the total angular momentum, commutes with the Hamiltonian of the Dirac equation and consequently it is a conserved quantity. Therefore, the spin arises naturally as a direct consequence of requiring the spinor field to satisfy the Dirac equation.

2.5.3 Feynman propagator

For interactions of fermions, an inhomogeneous equation is considered just like for scalar fields in Section 2.3.5:

$$(i\gamma^\mu\partial_\mu - m)\psi(x) = J(x). \quad (2.57)$$

The propagator $S(x - x')$ is introduced as a Green Function that satisfies the equation

$$(i\gamma^\mu\partial_\mu^x - m)S(x - x') = \delta^4(x - x'). \quad (2.58)$$

$S(x - x')$ is defined as

$$S(x - x') = \int \frac{d^4p}{(2\pi)^4} e^{-ip \cdot (x - x')} S_F(p), \quad \text{where} \quad (2.59)$$

$$S_F(p) = \frac{\not{p} + m}{p^2 - m^2 + i\varepsilon}. \quad (2.60)$$

$S_F(p)$ is known as the Feynman propagator, and just like for the scalar field propagator, the matrix elements of $S_F(x - x')$ can be written in terms of the field operators [8] in the form:

$$iS_{F\alpha\beta}(x - x') = \langle 0 | \mathcal{T} [\psi_\alpha(x) \bar{\psi}_\beta(x')] | 0 \rangle, \quad (2.61)$$

where the time-ordered products for the fields are

$$\mathcal{T} [\psi_\alpha(x) \bar{\psi}_\beta(x')] \equiv \begin{cases} \psi_\alpha(x) \bar{\psi}_\beta(x') & \text{if } t > t' \\ -\bar{\psi}_\beta(x') \psi_\alpha(x) & \text{if } t' > t. \end{cases} \quad (2.62)$$

2.6 Group theory

As symmetries allow to constrain the space of possible solutions, it can significantly reduce the number of potential Lagrangians that describe a particular physical interaction. Symmetries constitute groups of transformations that leave the Lagrangian unchanged. Groups

are the key to describe particles and its interactions as properties of these elementary particles are linked to the structure of Lie groups and Lie algebras.

A group G is a set of elements with a definite operation that satisfy the following conditions.

1. Closure: If A, B are elements of the group G then the product, $A B = C$ must be as well.
2. Associativity: For any three elements, $(AB)C = A(BC)$.
3. Identity element: There must exist a unit element 1 such that $1A = A1 = A$. For all elements of the group A .
4. Inverse element: For every element A there exists an inverse A^{-1} such that $A^{-1}A = AA^{-1} = 1$.

In general, the elements of a group do not need to commute, and so, if $AB \neq BA$, the group is called noncommutative or nonabelian group, which are of great interest as just as in quantum mechanics many important operators that do not commute carry important information as momentum or position.

2.6.1 Lie Groups

Lie groups are necessarily infinite, have one or more continuous parameters [11] and the group operation is an analytical function.

2.6.1.1 Group Representation

When working with groups it is useful to determine an specific representation as operations and members of the group are abstract. Therefore, by using the group representation they are transformed to a convenient format that is calculable. A common representation is expressing members of the group as square matrices M .

Some common Lie Groups are denoted using the following symbols:

1. **Special (S)**: Groups in which the determinant of the matrix is 1.
2. **Unitary (U)**: Formed by $n \times n$ unitary matrices i.e. matrices in which the inverse of the complex-valued matrix is equal to the Hermitian transpose: $MM^\dagger = 1$ [11].
3. **Orthogonal (O)**: Formed by $n \times n$ orthogonal matrices, which are matrices such that its inverse equals its transpose: $M^T M = M M^T = 1$

Any element of a Lie group can be expressed as

$$M(\theta_1, \theta_2, \dots, \theta_n) = \exp \left(i \sum_{i=1}^n \theta_i F_i \right) \quad (2.63)$$

where $n = N^2 - 1$ for the $SU(N)$ group and F_i are called the generators of the group. These generators satisfy the commutation relations called a Lie algebra

$$[F_i, F_j] = i f_{ijk} F_k, \quad (2.64)$$

where f_{ijk} correspond to structure constants. The physical interpretation of these generators is that each generator will ultimately give rise to a new particle, which will be a mediator particle. i.e a boson [11].

2.7 QED

ME FALTA ESTE COMENTARIO

QED is a gauge theory based on the symmetry $U(1)$ which refers to a charge conservation due to a symmetry of a phase transformation. The Lagrangian and equations of motion for the electromagnetic field are, respectively,

$$\mathcal{L} = -\frac{1}{4} F_{\mu\nu} F^{\mu\nu} - J^\mu A_\mu \quad \text{and} \quad \partial_\mu F^{\mu\nu} = J^\nu, \quad (2.65)$$

here due to the gauge invariance property of the theory neither the Lagrangian nor the equations of motion change under local transformations [8].

Nonetheless, QED is the quantized theory of interacting fermions and photons, so the Lagrangian developed includes the contributions of the locally gauge invariant Dirac Lagrangian, which describes fermions, and the gauge electromagnetic Lagrangian (2.65). We want to have an invariant Lagrangian under a local $U(1)$ transformation in which the symmetry is:

$$\psi(x) = e^{i\alpha(x)} \psi(x). \quad (2.66)$$

The locally gauge invariant Dirac Lagrangian is obtained by adding to the Lagrangian corresponding to the Dirac Equation (2.51):

$$\mathcal{L} = \bar{\psi}(i\not{D} - m)\psi, \quad (2.67)$$

which is invariant under global U(1) transformations, a term of the form

$$\mathcal{L}_I = -q\bar{\psi}\gamma^\mu A_\mu\psi, \quad (2.68)$$

which promotes the global U(1) symmetry to a local symmetry, and combining this new locally gauge invariant Dirac lagrangian with the electromagnetic Lagrangian one obtains that:

$$\mathcal{L}_{QED} = \bar{\psi}(i\gamma^\mu D_\mu - m)\psi - \frac{1}{4}F_{\mu\nu}F^{\mu\nu} \quad \text{where,} \quad (2.69)$$

$$D_\mu\psi = \partial_\mu\psi + iqA_\mu\psi, \quad (2.70)$$

$$F_{\mu\nu} = \partial_\mu A_\nu - \partial_\nu A_\mu. \quad (2.71)$$

And the gauge field transforms as:

$$A_\mu \longrightarrow A_\mu - \frac{1}{q}\partial_\mu\alpha. \quad (2.72)$$

2.8 EWT

2.8.1 Weak interaction

For the weak force all hadrons and leptons take part in the interaction, it was first discovered in nuclear β -decays back in 1896 by Becquerel, in this process of decay, the energy of the emitted rays, i.e. of the electrons, was continuous and there was no sign of other particles. Namely, the law of conservation of energy seemed to be violated. Consequently, Pauli proposed in 1930 that a yet unknown particle (neutrino) carries away the missing energy. In 1934, taking into account Pauli's neutrino hypothesis, Fermi proposed the first weak interaction theory to explain the phenomenon, and its formalism was made in analogy with the electromagnetic interaction [1].

FALTA

The theory consist of a SU(2) symmetry in which there is a nonlinear interaction, characteristic of a nonabelian gauge theory. It is characteristic of the weak interaction to violate parity, the carriers of this force, the W^\pm bosons, have large masses so, if the weak force respects the gauge principle, the symmetry is broken and as a result the theory is unrenormalizable leading to the discussion of the Higgs field. As mentioned in Section 1 the three left-handed doublets are (e, ν_e) , (μ, ν_μ) , (τ, ν_τ) , where they do not mix with each other which is commonly referred to as lepton flavor conservation, and here emerges also a new conserved charge called the isospin.

(a transformation in which position coordinates are inverted)

The Lagrangian associated with a SU(2) symmetry for fermions turns out to be:

$$\mathcal{L}_{SU(2)} = \bar{\psi}(i\gamma^\mu D_\mu - m)\psi - \frac{1}{4}\mathbf{G}_{\mu\nu}\mathbf{G}^{\mu\nu} \quad \text{where,} \quad (2.73)$$

$$D_\mu = \partial_\mu - \frac{i}{2}g\boldsymbol{\sigma} \cdot \mathbf{W}_\mu(x), \quad (2.74)$$

$$\mathbf{G}_{\mu\nu} = \partial_\mu \mathbf{W}_\nu - \partial_\nu \mathbf{W}_\mu + g(\mathbf{W}_\mu \times \mathbf{W}_\nu) \quad (2.75)$$

where D_μ is the covariant derivative, \mathbf{W}_μ is the gauge field, g corresponds to the "charge" of the theory, i.e how strongly the gauge field \mathbf{W}_μ interacts with ψ , and $\boldsymbol{\sigma}$ are the Pauli matrices. It was discovered by Wu [11] that the weak sector of the SM violates parity. This was discovered thanks to experiments that showed that there was a "preference" in the quirality of particles, an asymmetry in the angular distribution of the decay particles which means that parity is violated in the decay. This preference is caused by the absence of right-handed neutrinos [1].

The weak theory has very similar interactions as the ones in the electromagnetic field, which inspired physicist to pursue a self-consistent mathematical framework as the one modeled on QED, which eventually led to the unified theory of the electromagnetic and weak forces called the electroweak theory, this theory thus consists of a $SU(2)_L \times U(1)_Y$ symmetry [1].

FALTA

As the charge now includes isospin, we can define the total electric charge via the Gell-Mann-Nishijima relation as

$$Q = I_3 + \frac{Y}{2}, \quad (2.76)$$

in which I_3 corresponds to the third component of the isospin (I) and Y to the weak hypercharge. The force carriers associated with this theory are the three gauge vector bosons W^\pm and Z^0 and the photon γ . Due to the fact that there are no right-handed neutrinos the fermion fields can be written as:

$$\psi = \begin{pmatrix} L \\ R \end{pmatrix}, \quad \text{where} \quad L = \begin{pmatrix} \nu_e \\ e_L \end{pmatrix}, \quad R = e_R. \quad (2.77)$$

As there are two internal symmetries in the EWT it is needed to replace the covariant derivatives as

$$U(1) : D_\mu \psi = \partial_\mu \psi - \frac{i}{2} g' Y B_\mu(x) \psi, \quad (2.78)$$

$$SU(2) : D_\mu \psi = \partial_\mu \psi - ig I \boldsymbol{\sigma} \cdot \mathbf{W}_\mu(x) \psi, \quad (2.79)$$

or in terms of L and R:

$$D_\mu L = \partial_\mu L - \frac{i}{2} g \boldsymbol{\sigma} \cdot \mathbf{W}_\mu L + \frac{i}{2} g' B_\mu L, \quad (2.80)$$

$$D_\mu R = \partial_\mu R + ig' B_\mu R. \quad (2.81)$$

where g and g' correspond to the coupling constants to the isospin and the hypercharge respectively. When writing the full Lagrangian, the right-handed electrons (e_R) have no partner giving rise to a singlet term in our Lagrangian, which becomes

$$\begin{aligned} \mathcal{L}_{EWT} = & \bar{R} i \gamma^\mu (\partial_\mu + ig' B_\mu) R + \bar{L} i \gamma^\mu \left(\partial_\mu - \frac{i}{2} g \boldsymbol{\sigma} \cdot \mathbf{W}_\mu + \frac{i}{2} g' B_\mu \right) L \\ & - \frac{1}{4} \mathbf{G}_{\mu\nu}^{(W)} \cdot \mathbf{G}^{(W)\mu\nu} - \frac{1}{4} F_{\mu\nu}^{(B)} F^{(B)\mu\nu}. \end{aligned} \quad (2.82)$$

2.8.2 The Higgs Mechanism

As one can see, this Lagrangian does not include a mass term and consequently it only describes massless fields, nevertheless mass can be put by hand but with the consequence that the gauge invariance gets broken and no renormalization can be made. This leads to the concept of spontaneous symmetry breaking (SSB) [14]. Nambu was the first one to introduce the idea of SSB into particle physics. This concept is fundamental in our theory, of course there is mass in the universe and hence we live in a broken symmetry universe and, in fact, all the particles we observe are a consequence of this symmetry breaking. As a consequence of SSB, the Higgs mechanism is introduced, which corresponds to the process in which fermions and bosons acquire mass by interacting with a new complex scalar field, called the Higgs field [1][2].

In a gauge theory, breaking a continuous symmetry results in a massless excitation known as the Goldstone boson, which can be removed becoming massive through the combination with a gauge field [2]. In other words, fermions and bosons acquire mass by interacting with the Higgs field and in this process a component of the Higgs field is converted to a component of the gauge field to make it massive i.e. "removing" the Goldstone boson

and giving rise to massive fields [1]. In consequence, our universe is permeated by a symmetry-broken field (Higgs field) and the mass of all particles is determined by how strongly they interact with it. Interaction with the Higgs field are mediated by a quanta, known as the Higgs boson.

The Higgs field is a complex scalar field as mentioned in Section 2.3 which has four components that can be expressed as:

$$\phi = \begin{pmatrix} \phi^+ \\ \phi^0 \end{pmatrix}, = \begin{pmatrix} \phi_3 + i\phi_4 \\ \phi_1 + i\phi_2 \end{pmatrix}. \quad (2.83)$$

It is necessary to know how this field transforms under U(1) and SU(2) transformations in order to include it in our theory i.e. include it in the EWT Lagrangian of Equation (2.82). Given the Higgs field has a weak hypercharge of +1 and isospin 1/2 it follows from Equations (2.78) and (2.79) that

$$D_\mu \phi = \partial_\mu \phi - \frac{i}{2} g \boldsymbol{\sigma} \cdot \mathbf{W}_\mu \phi - \frac{i}{2} g' B_\mu \phi. \quad (2.84)$$

With the covariant derivative of the Higgs field it is possible to write its Lagrangian \mathcal{L}_ϕ and its interaction Lagrangian \mathcal{L}_I with electrons and neutrinos as:

$$\mathcal{L}_\phi = (D^\mu \phi)^\dagger (D_\mu \phi) + \frac{\mu^2}{2} \phi^\dagger \phi + \frac{\lambda}{4} (\phi^\dagger \phi)^2, \quad (2.85)$$

$$\mathcal{L}_I = -G_e (\bar{L} \phi R + \bar{R} \phi L). \quad (2.86)$$

Where G_e is the coupling constant of the interaction. As any other Lagrangian the the Higgs Field Lagrangian \mathcal{L}_ϕ is of the form $\mathcal{L} = K - U$, and so the Higgs potential has the form $U = \frac{\mu^2}{2} \phi^\dagger \phi + \frac{\lambda}{4} (\phi^\dagger \phi)^2$ [2]. It can be shown that higher order terms generate divergences. When taking $\mu^2 < 0$ this potential does not have a minimum at $\phi = 0$, the minimum of this potential is actually at

$$|\phi| = \sqrt{\frac{-\mu^2}{\lambda}}, \quad (2.87)$$

giving as a result a Mexican Hat potential as the one shown in Figure 2. Which implies the breaking of the symmetry and gives masses to the elementary particles.

Putting together the Higgs Lagrangian (Equation (2.85)), its interaction term (Equation 2.86)) and the EWT Lagrangian (Equation (2.82)) the complete Lagrangian now becomes:

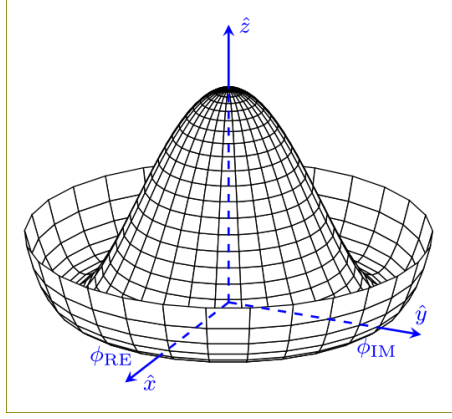


Figure 2: The potential of the higgs Field.

$$\begin{aligned} \mathcal{L} = & \bar{L}i\gamma^\mu D_\mu L + \bar{R}i\gamma^\mu D_\mu R + (D^\mu \phi)^\dagger (D_\mu \phi) + \frac{\mu^2}{2} \phi^\dagger \phi - \frac{\lambda}{4} (\phi^\dagger \phi)^2 \\ & - G_e (\bar{L}\phi R + \bar{R}\phi^\dagger L) - \frac{1}{4} \mathbf{G}_{\mu\nu}^{(W)} \cdot \mathbf{G}^{(W)\mu\nu} - \frac{1}{4} F_{\mu\nu}^{(B)} F^{(B)\mu\nu} \end{aligned} \quad (2.88)$$

To obtain the physical particles we observe experimentally it is necessary to make a transformation to the fields presented on the theory such that:

$$W^+ = \frac{(-W^1 + iW^2)}{\sqrt{2}}, \quad W^- = \frac{(-W^1 - iW^2)}{\sqrt{2}}, \quad W^0 = W^3, \quad (2.89)$$

where W_1, W_2 and W_3 are the components of the previous presented \mathbf{W}_μ . Additionally, we have that B and W^3 are not eigen states of the mass and therefore their mass matrix is not diagonal, for this we carry out a rotation which allows us to obtain the physical particles γ and Z^0 so that our mass matrix is diagonal.

$$\begin{pmatrix} \gamma \\ Z^0 \end{pmatrix} = \begin{pmatrix} \cos \theta_W & \sin \theta_W \\ -\sin \theta_W & \cos \theta_W \end{pmatrix} \begin{pmatrix} B \\ W_3 \end{pmatrix} \quad (2.90)$$

2.9 QCD

Lastly, QCD emerges from studying the strong force, responsible to bind quarks together to form hadrons. The so called color charge, an intrinsic quantum property of quarks, is the source of this type of interaction, such as the electric charge is responsible for electromagnetic processes. The discovery of the color degrees of freedom was the key to understand this kind of interaction. The boson mediator of this force is the gluon, its mass is considered to be zero just like the photon. According with the theory, there are eight gluons, considered the generators of the $SU(3)$ symmetry group. In summary, QCD

theory, involves three different type strong charges (known as colors: red, green, blue), eight gluons, associated as generators of the corresponding SU(3) group, this last being non-abelian. Experimentally, quarks are always found in bound states, forming hadrons, as explained before. This last feature is a consequence of the characteristics of the strong potential [15]. Therefore, stored potential energy between them increases with distance and quarks cannot be isolated individually. We call this phenomenon "confinement". Along with the color charge, other properties arose with this theory, Gell-Mann and Nishijima introduced the baryon number (B), which combined with the strangeness (S) leads to another fundamental quantity, the strong hypercharge:

$$Y = B + S, \quad (2.91)$$

where Y corresponds to the same hypercharge presented in equation (2.76). Since the characteristics of the strong force and weak force are very much alike, the color force is expected to obey the same mathematical framework as that of the electromagnetic force, namely gauge theory. The difference lies in the number of charges. There are three color charges (R, G, B) in our QCD theory, which generate the strong force with equal strength and the emission or absorption of the force carrier changes the color [1]. The Lagrangian associated with our SU(3) symmetry is, in form, the same as SU(2) which is in equation (2.73) but this time we are working on a different group and the form of the tensor $F^{\mu\nu}$ is different. The covariant derivative would also change and there is introduced an asymptotic freedom consequence of the nonlinear gluon coupling, which means that the more separated quarks get the stronger the interaction becomes. This lead to the confinement phenomenon described earlier, which in terms of potential can be written as

$$V(r) = \frac{a}{r} + br. \quad (2.92)$$

2.10 Interactions

After discussing free fields it is necessary to go over a more realistic approach in which interactions of the fields are considered, here particles can be scattered, created or destroyed. The possibles interactions depend on the type of fields interacting, the interaction in general is described by the interaction Lagrangian \mathcal{L}_I which involves the interacting fields and the coupling constants. It is the nature of the interaction that defines a specific theory, for example, any theory with a scalar and a fermion field interacting is called Yukawa theory. The interactions with four fermionic field operators are called Fermi interactions, or sometimes 4-fermion interactions. With the scalar field, we can have a $\lambda\phi^4$ theory where the only interaction is associated with the ϕ^4 term. Discussion of these and other interactions requires a general framework to deal with interacting fields , which leads to

the discussion of the S Matrix [8].

2.10.1 The S matrix

The idea with working on interacting theories is to be capable of predicting the behavior of the system from its initial conditions, i.e. being capable of knowing all possible final states ($|f\rangle$) given an initial state ($|i\rangle$). This can be achieved through the use of the S matrix, which corresponds to the amplitude of transition from ($|i\rangle$) to an specific ($|f\rangle$):

$$\langle f|S|i\rangle = S_{fi} \quad \text{where,} \quad \sum_f |S_{fi}|^2 = 1, \quad (2.93)$$

where S in general is defined as:

$$S = \mathcal{T} \left[\exp \left(-i \int_{-\infty}^{\infty} dt H_1(t) \right) \right], \quad (2.94)$$

and since

$$H_I(t) = \int d^3x \mathcal{H}_I(x). \quad (2.95)$$

We can also write the definition of the S matrix as:

$$S = \mathcal{T} \left[\exp \left(-i \int d^4x \mathcal{H}_1(x) \right) \right] \quad \text{with,} \quad SS^\dagger = S^\dagger S = 1. \quad (2.96)$$

Usually, when working with the S matrix we work with its expansion

$$S = \sum_{n=0}^{\infty} S^{(n)} \equiv \sum_{n=0}^{\infty} \frac{(-i)^n}{n!} \int \dots \int d^4x_1 \dots d^4x_n \mathcal{T} [\mathcal{H}_1(x_1) \dots \mathcal{H}_1(x_n)] \quad (2.97)$$

The expansion of the S -matrix is of great importance, since it contains the complete information about all collision processes to any order of perturbation theory and with the use of Wick's theorem the terms in this expansion can be written as a sum of normal products. Nonetheless, S_{fi} can be also written in terms of its **Feynman amplitude**, which, as we will see in the following Chapters, we can find directly from the Feynman graphs, rather than proceeding from Wick's theorem, making calculations far more compact and straight forward.

2.10.2 Cross Sections and Feynman Amplitude

The S matrix element between the states $|i\rangle$ and $|f\rangle$ can be expressed as

$$S_{fi} = \delta_{fi} + i(2\pi)^4 \delta^4 \left(\sum_i p_i - \sum_f p_f \right) \prod_i \frac{1}{\sqrt{2E_i V}} \prod_f \frac{1}{\sqrt{2E_f V}} \mathcal{M}_{fi} \quad (2.98)$$

where we have a term for when the initial and partial states are the same, a δ function related to the conservation of 4-momentum in the process, a $\frac{1}{\sqrt{2EV}}$ for each particle on the initial or final state and the Feynman amplitude $i\mathcal{M}_{fi}$ which contains the specific information on the interaction on the specific process, both the decay rate of a particle or a scattering process' cross section depend on this element of the S matrix (\mathcal{M}_{fi}).

Cross section: The cross section refers to the probability that a specific process will take place, it is denoted as σ and classically it is defined as

$$\sigma = \oint_{4\pi} \frac{d\sigma}{d\Omega} d\Omega = \int_0^{2\pi} \int_0^\pi \frac{d\sigma}{d\Omega} \sin\theta d\theta d\varphi, \quad \text{where:} \quad (2.99)$$

$$\frac{d\sigma}{d\Omega} = \frac{b}{\sin\theta} \left| \frac{db}{d\theta} \right| \quad (2.100)$$

is the differential cross section, and the parameter b , Ω (the solid angle) and θ are defined as shown in Figure 3.

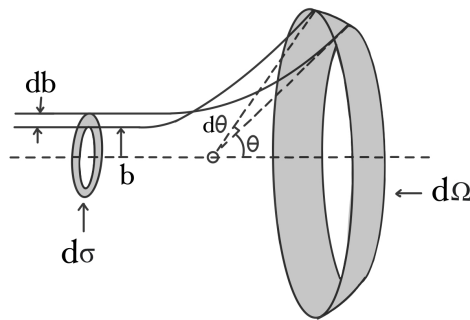


Figure 3: Diagram of scattering parameters where the angle of scattering is determined by impact parameter $b(\theta)$.

Further more, as explained before the cross section of a specific process can be written

in terms of the Feynman amplitude, it is related by

$$\sigma = \frac{1}{v_{\text{rel}}} \frac{1}{4E_1 E_2} \int \prod_f \frac{d^3 p_f}{(2\pi)^3 2E_f} (2\pi)^4 \delta^4 \left(\sum_i p_i - \sum_f p_f \right) |\mathcal{M}_{fi}|^2 \quad (2.101)$$

where v_{rel} correspond to the relative velocity of the particles (incident particle and target particle) $v_{\text{rel}} = \sqrt{(p_1 \cdot p_2)^2 - m_1^2 m_2^2} / E_1 E_2$. This leads to the use of **Feynman diagrams** as a way of interpreting the terms of the Feynman amplitude \mathcal{M}_{fi} that would normally be obtained in the Wick expansion.

2.10.3 Feynman Rules

As presented in Chapter 2.10.1, the transition amplitude for scattering, which corresponds to the sum of each possible interaction over all possible intermediate particles, is given as the matrix element of the S matrix between the initial and the final states of the quantum system. The order of the perturbation expansion is given by the amount of times our interaction Hamiltonian (\mathcal{H}_I) acts, and this time-dependent perturbation theory is known as the *Dyson series* which allow us to define the S matrix as in Equation 2.96. The Dyson series can be alternatively rewritten as a sum over Feynman diagrams, which provide deep physical insight into the nature of particle interactions. A Feynman diagram represents a term of the Wick expansion and give a simple way to calculate the amplitudes of scattering processes. When working with Feynman diagrams, each process that can occur is related with a diagram and these are constructed by following the Feynman rules which help us find the expression necessary to calculate the scattering cross section for a specific process.

Some of the basic Feynman rules are:

- **External lines:** The external lines of the diagram correspond to the initial and final particles, all the possible external lines are shown in Figure 4.

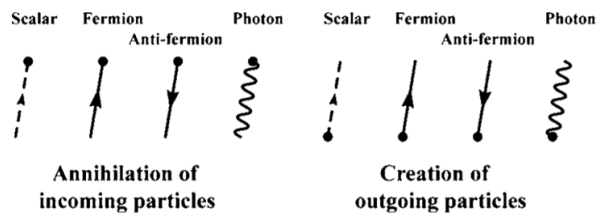


Figure 4: External lines of Feynman diagrams for the different possible final and initial states (taken from [1]).

For each external line the wave functions assigned are

Table 1: Wave functions associated with each particle

scalar boson	$\phi^\dagger(x) \rightarrow e^{ik' \cdot x}$	$\phi(x) \rightarrow e^{-ik \cdot x}$
electron	$\bar{\psi}(x) \rightarrow \bar{u}(p') e^{ip' \cdot x}$	$\psi(x) \rightarrow u(p) e^{-ip \cdot x}$
positron	$\psi(x) \rightarrow v(p') e^{ip' \cdot x}$	$\bar{\psi}(x) \rightarrow \bar{v}(p) e^{-ip \cdot x}$
photon	$A_\mu(x) \rightarrow \varepsilon_\mu(k')^* e^{ik' \cdot x}$	$A_\mu(x) \rightarrow \varepsilon_\mu(k) e^{-ik \cdot x}$

- **Internal lines:** The internal lines of a diagram correspond to particles associated with propagators. Internal lines associated with different particles are presented in Table 2

Table 2: Propagator terms associated with each particle.

scalar	$i \Delta_F(k^2) = i/(k^2 - m^2 + i\varepsilon)$
photon	$i D_F(k^2) = -i g_{\mu\nu}/(k^2 + i\varepsilon)$
electron	$i S_F(k^2) = i(p + m)/(p^2 - m^2 + i\varepsilon)$
massive vector	$i \Delta_F^{\mu\nu}(k^2) = -i (g^{\mu\nu} - k^\mu k^\nu/m^2)/(k^2 - m^2 + i\varepsilon)$

We start by writing the momentum in Feynman diagram with the momentum of the external lines, and then start putting the momentum of the internal lines. At any stage, if the momentum of an internal line is determined by the momentum of the external lines and of the internal lines whose momentum have already been assigned, also the lines drawn in the Feynman diagrams for those internal lines are shown in Figure 5:

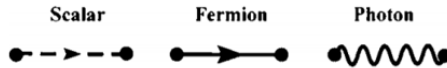


Figure 5: Internal lines of Feynman diagrams for the different possible propagators (taken from [1]).

- **Loop lines and vertices:** After adding the momentum of all external and internal lines for each loop found in the process a term of

$$\int \frac{d^4 q}{(2\pi)^4} \quad (2.102)$$

is added and if the loop is a fermion loop a (-1) is added due to the anticommutative nature of fermions.

For vertices, the rules are not general as they depend on the theory and the interaction, for example whether we have a QCD vertex or a QED vertex the terms are differently

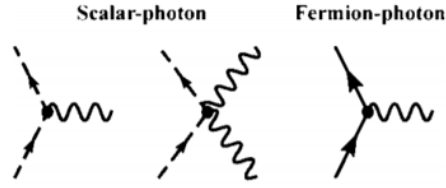


Figure 6: Examples of vertices of a Feynman diagram (taken from [1]).

put. The vertices correspond to the points in which external and internal lines merge, as shown for example in Figure 6, in each vertex there must be conservation of momentum, charge, energy, angular momentum, lepton number (L) ($L_{e^-}, \nu_e = +1$ and $L_{e^+}, \bar{\nu}_e = -1$ and similar for muons and taus), baryon number (B) ($B = \frac{1}{3} (n_q - n_{\bar{q}})$) and strangeness ($S = -(n_s - n_{\bar{s}})$), which is associated with the presence of a strange quark and emerged to explain the fact that certain particles, such as the kaons or the hyperons, were created easily in particle collisions, yet decayed much more slowly than expected [16], and parity, where the last two are not conserved on weak interactions.

3 Beyond the Standard Model

Several theoretical models have been proposed in order to address the open problems of the SM. There are some hints that lead to the concept of a unified theory, for example, the SM is constructed by the three gauge symmetries explained in Section 2 ($SU(3)_C \times SU(2)_L \times U(1)_Y$). The coupling constants of each of these symmetries vary with the energy at which they are measured and around $\sim 10^{16}$ GeV these couplings become approximately equal, leading to the idea that these symmetries can be unified into one single gauge symmetry, i.e. one gauge group G with one single coupling constant. Based on this concept, a group of theories called grand unified theories (GUTs) emerges, where it is expected that at higher energies QCD should unite with EWT in much the same way that the electromagnetism unites with the weak force to create the EWT. These theories are usually based on higher-dimensional constructions such as string compactifications, where the most common symmetries considered involve $SU(5)$ or $SO(10)$ groups [17].

3.1 Z' physics

One common feature of several SM extensions proposed, that involve enhanced gauge symmetries, is the prediction of additional gauge bosons such as the W' and Z' [18]. An important feature of these models is that these new bosons are relevant to the low energy charged and neutral current processes, respectively [19]. Also, a GUT containing a Z' , for example, predicts many new particles such as additional (exotic) fermions, additional charged gauge bosons or additional Higgs bosons. In the simplest case of a $SO(10)$ GUT, the only additional fermion is one right-handed neutrino [20].

The Z' is expected to be a new resonance with properties similar to the Z^0 SM boson. In general, the Z' boson is a massive, electrically-neutral, and color-singlet hypothetical particle of spin 1. Z' arises in many unification theories: it is proposed as a heavy mass eigenstate in strongly interaction theories, such as non-commuting extended technicolor [21][22]. These are dynamical theories that attempt to explain fermion masses based on interactions with heavy techni-fermion (fermions belonging to a complex representation of a new gauge technicolor group $SU(N_{TC})$) [23] condensates by the exchange of a massive gauge bosons [24]. In other models with extra dimensions, such as the Randall-Sundrum model [25], the Z' boson arises as the lowest Kaluza-Klein excitation [26] of a Z^0 boson [27] [28]. Those extra dimensional models are based on the formulation that the four dimensional world around us arises from the compactification of a, for example, curved 5D geometry,

and excitations of these higher dimensions can be detected through a Kaluza-Klein resonance [26]. Z' bosons also arise in Little Higgs [29], Hidden Valley [30] or 331 models [31].

A commonly studied model involving the Z' is the Left-Right Symmetric Model (LRM), based on the gauge group $SU(2)_L \times SU(2)_R \times U(1)_{B-L}$ [20]. These models try to solve some of the problems of the SM such as Parity Violation in the weak interactions, and non-zero neutrino masses implied by the experimental evidence of neutrino oscillation [32]. The LRMs add an additional group $SU(2)_R$ to the SM, where W' is the right-handed counterpart to the left-handed SM W^\pm .

Some others highly motivated models where a Z' boson emerges are those that involve additional $U(1)'$ gauge symmetries, called Sequential Standard models (SSM) [33], have been studied extensively including detections at the LHC [34]. Some models that arise also from the inclusion of $U(1)$ symmetries include the E_6 GUT, B-L model, or the minimal SM extension $SU(3)_c \times SU(2)_L \times U(1)_Y \times U'(1)$. In the E_6 model, for example, due to the decomposition $E_6 \rightarrow SO(10) \times U(1)_\psi \rightarrow SU(5) \times U(1)_\chi \times U(1)_\psi$ two extra $U(1)'$ symmetries emerge. The mixing of these extra $U(1)'$ symmetries lead to a new gauge boson: $Z'(\theta) = Z'_\psi \cos \theta + Z'_\chi \sin \theta$, where the mixing angle θ determines the coupling to fermions [20]. In general the most common Z' decays are leptonic decay or b decays as shown in Figure 7.

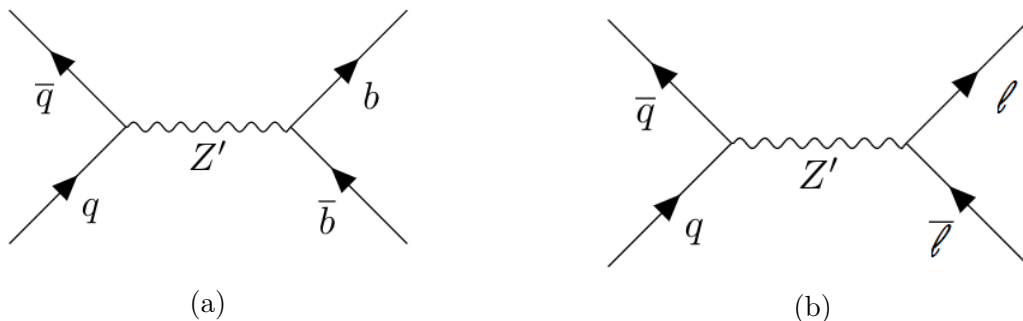


Figure 7: Representative Feynman diagrams of expected Z' decays.

The Z' boson is a heavier partner of the SM Z boson. Therefore, physically, it is described by the Proca Equation 2.45. When considering the simplest extension of an additional $U(1)'$ symmetry to the electroweak sector, the Z' naturally emerges. Then, the neutral part of the interaction Lagrangian is:

$$\mathcal{L} = -e J_E^\mu A_\mu - g_0 J_0^\mu Z_\mu^0 - g_1 J_1^\mu Z_\mu^1. \quad (3.1)$$

Nonetheless, the mixing between the Z and the Z' masses is not forbidden [35] so the

mass Lagrangian in general is written as:

$$\mathcal{L}_Z^{\text{mass}} = \frac{1}{2}m_Z^2 Z_\mu Z^\mu + \frac{1}{2}m_{Z'}^2 Z'_\mu Z'^\mu + \text{mixing} , \quad (3.2)$$

which can be seen more explicitly if written in a matrix format such that the mixing terms are the ones that appear out of the diagonal of the matrix:

$$\mathcal{L} = \begin{pmatrix} Z & Z' \end{pmatrix} \begin{bmatrix} m_Z^2 & \delta M^2 \\ \delta M^2 & m_{Z'}^2 \end{bmatrix} \begin{pmatrix} Z & Z' \end{pmatrix}^T . \quad (3.3)$$

Therefore, the Z and Z' bosons are not the mass eigenstates and analogously with in EWT there exists a change of basis such that the mass matrix is diagonal. The diagonal matrix is obtained by performing a rotation, which yield the associated eigenstates Z_1 and Z_2 :

$$\begin{pmatrix} Z_1 \\ Z_2 \end{pmatrix} = \begin{pmatrix} \cos \theta_M & \sin \theta_M \\ -\sin \theta_M & \cos \theta_M \end{pmatrix} \begin{pmatrix} Z \\ Z' \end{pmatrix} . \quad (3.4)$$

The importance of searches for new heavy gauge bosons, and properties like their masses, lies in the role it plays in the development of new theories, because, in case of a discovery, the search for such particles in different decay channels will help to comprehend and go further in the underlying theory providing information on the GUT group itself and on its symmetry breaking [20][36]. The mass of the Z' is not constrained by theory, a priori, it can be anywhere between E_{weak} and E_{GUT} (which is the energy at which the strong and electroweak interactions can be merged into a simple group G) but it is expected to have a mass of the order of one TeV.

At the LHC, searches for additional neutral gauge bosons can be performed in a variety of processes. Lepton decays are particularly attractive because these decays correspond to very clean channels to look for: a peak in the invariant mass distribution of the lepton pairs [17][37]. The importance of the experiments directed at the LHC is that through them, particles and their interactions can be identified. Even before selecting a theory to work on, accurate measurements of the corresponding parameters of a certain particle (masses, couplings, spin, charges) can be made, giving useful information about the particles being studied independent of the model or theory in which it appears [38].

For the study of Z' production at the LHC we are going to consider two different final states (channels), shown in Figure 8. We will examine different values of $M_{Z'}$ to understand the behavior of the cross section, under difference coupling scenarios. The background processes associated with SM event with similar final states and the hypothetical signals, will be statistically studied to determine the preliminary sensitivity of a search at the

LHC.

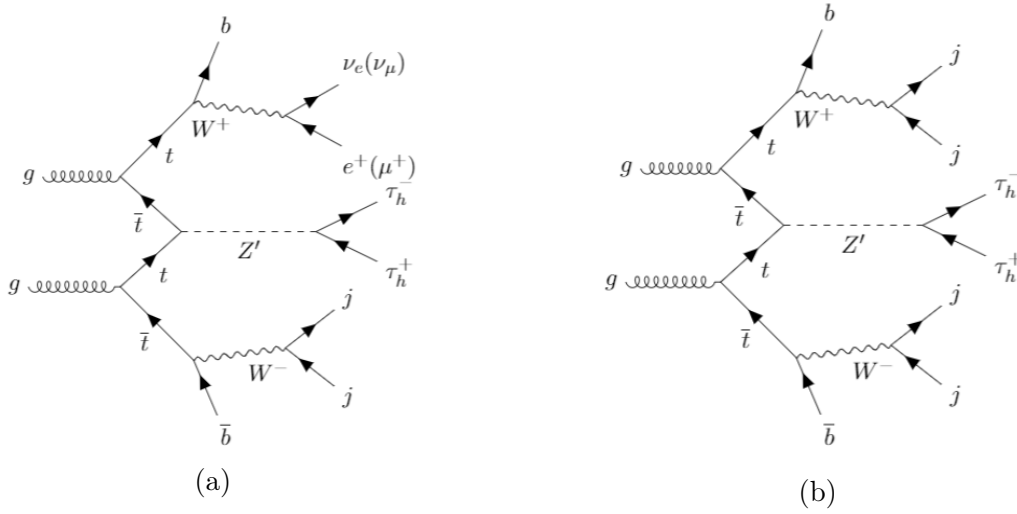
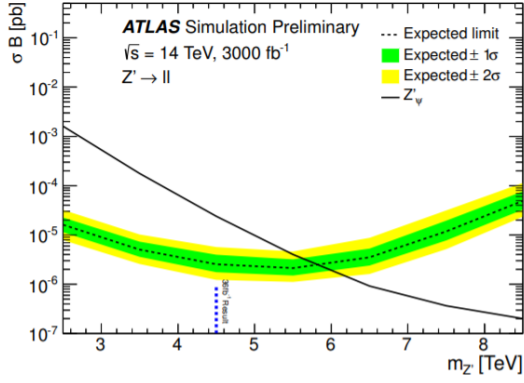


Figure 8: Diagram (8a) shows a process of $Z' \rightarrow \tau_h^+ \tau_h^-$ obtaining 2 b, $2\tau_h$ 1 e or , missing energy associated with the neutrinos (ν_e or ν_μ) and 2 jets. Diagram (8b) shows this same process of decay of the Z' but obtaining 2 b, $2\tau_h$ and 4 jet. τ_h represents τ particles that decay hadronically.

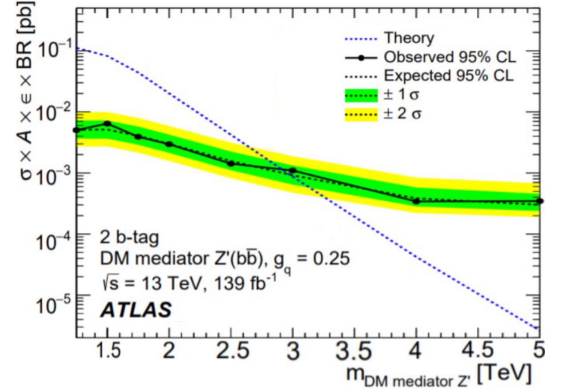
3.2 Recent results regarding Z' production

Some of the latest results obtained at the ATLAS experiments at the LHC involving Z' production, show the current limits of the possible values of $M_{Z'}$ (see [36], [39] and [40]). It has been observed that for SSM Z' and the E_6 model Z'_ψ with dilepton final states and $\sqrt{s} = 13$ TeV collision, masses up to 6.5 and 5.8 TeV respectively are excluded. It is important to mention that these exclusion limits were reassured in final states with light leptons, muons and electrons, with no preferential coupling to third generation leptons. For dark matter (DM) models, Z' production assuming Z' decays into two b-jets for $\sqrt{s} = 13$ TeV excludes masses up to 2.9 TeV [39]. Lastly, upper limits are set for the Z'_{TC2} boson in $t\bar{t}$ decay in the topcolor-assisted-technicolor model [41] [42], resulting in exclusion of masses up to 4.7 TeV with a proton-proton collision at $\sqrt{s} = 13$ TeV. These studies mark limits for the search of this new neutral gauge boson, allowing us to go further into the energy scale. The results shown in [36] [39] and [40] present the graphs given in Figure 9, in which the analysis of the behavior of the cross-section vs $M_{Z'}$ showed that no significant deviation from the expected background is observed, all the data obtained lies in the regions of maximum likelihood up to 2σ from the expected values, in regions corresponding to lower cross-sections that the predicted value by the theory, and consequently it gives no sign of new physics.

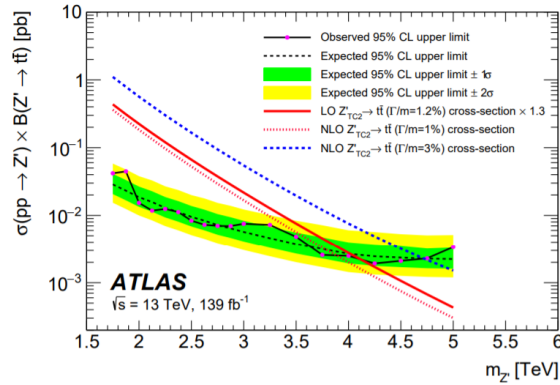
One remarkable indication of new physics is the observations made at the LHCb (Large



(a) Observed and expected upper limits on the cross section for the E_6 model with a leptonic decay of the Z' .



(b) Observed and expected upper limits on the cross section times branching ratio for the DM model for a decay of the Z' to $b\bar{b}$.



(c) Observed and expected upper limits on the cross section times branching ratio for the TC2 model for LO and NLO of the Z' decay to $t\bar{t}$.

Figure 9: Diagrams 9a, 9b and 9c show the cross-section obtained for different masses of Z' for different BSM models (Images taken from [36] [39] and [40]).

Hadron Collider beauty experiment) that there is a time-dependent, matter–antimatter asymmetry in the decays of particles known as B_s^0 mesons into charged kaons, this is an indication of CP violation that suggests the existence of as-yet-unknown sources. Manifestations of this violation imply physics beyond the Standard Model due to the fact that observations at the LHC have shown a statistical significance of 6.7 standard deviations [43], which is beyond the threshold of 5 standard deviations, leading to the claim of new physics, where several models have been put forward as possible new explanations [44]. It is proposed that models involving Z' bosons that are associated with flavor-changing interactions can explain the excesses in the B_s^0 decays to kaons [43][44][45]. This asymmetry is a good indicator of new physics as the first time CP violation was observed, more than five decades ago, was precisely in particles called K^0 mesons (kaons) which presented anomalies, (like the B_s^0 particles do now), and this phenomena helped discover a significant amount of new physics and particles such as the top and bottom quarks.

4 Signal simulation and data analysis

Accurate simulations of the signal and background play an important part in the experiments developed at the LHC. Characteristic signatures usually have large SM backgrounds that need to be measured as they share the same final states as the processes studied. The SM backgrounds considered for our study, include the production of top quark pairs, $t\bar{t}$, production of top quark pairs in association with a Z boson, $t\bar{t}Z$, pairs of vector bosons (diboson): ZZ, WW, and WZ, and production of three vector bosons: WWW, WWZ, and WZZ.

4.1 Madgraph

It is important to perform an accurate model of the hypothetical production of a Z' boson under the LHC conditions. The correct modeling its production, including kinematics, cross-section, mass, angular distributions, among others, is important to probe these models against experimental data [46] [47]. For this, the events that are needed in order to study these properties are generated using MadGraph, which is a open source software written in Python that acts like a Monte Carlo (MC) event generator, producing all the associated matrix elements of the initial and final states under study. [38].

The signal and backgrounds simulations were made using MadGraph5 v2.9.2. One million events were generated for the process of $p p \rightarrow t \bar{t} Z'$ for the two different decays considered and shown in Figure 8 and the two most relevant backgrounds were considered: $t \bar{t} Z$, $t \bar{t}$, for which five million of events were generated to obtain more statistic on these processes. The results obtained include the cross section associated with each subprocess, the total cross section and the unweighted events file containing the final states information. The code lines generating these processes are shown below:

For the semileptonic channel:

```
mg5: generate p p > t t~ zp, zp > ta+ ta-), (t > b j j), (t~ > b~ vl l)
mg5: add process p p > t t~ zp, (zp > ta+ ta-), (t > b vl l), (t~ > b~ j j)
```

For the fully hadronic channel:

```
mg5: generate p p > t t~ zp, zp > ta+ ta-), (t > b j j), (t~ > b~ j j)
```

Higgs background:

```
mg5: generate p p > t t~ h, (h > ta+ ta-), (t > b j j), (t~ > b~ vl l)
```

```
mg5: add process p p > t t~ h, (h > ta+ ta-), (t > b vl l), (t~ > b~ j j)
```

Z or γ^* background:

```
mg5: generate p p > t t~ ta+ ta- /h, (t > b vl l), (t~ > b~ j j)
```

```
mg5: add process p p > t t~ ta+ ta- /h, (t > b j j), (t~ > b~ vl l)
```

All the processes generated included $vl = ve \ ve \sim \nu\mu \ \nu\mu \sim$ and $l = e+ \ e- \ \mu+ \ \mu-$. Different values of masses for the Z' boson were considered. We took a "low mass" range, in which we considered masses of 150 GeV, 200 GeV, 250 GeV and 300 GeV. On the other hand, for "high masses" scenario, masses of 350 GeV, 1000 GeV, 1500 GeV and 2000 GeV were considered. The cross sections associated with each process with a $\sqrt{S} = 13 \text{ GeV}$ are presented in Table 3.

Table 3: Signal cross sections calculated with MadGraph for all the masses of the Z' studied.

Process	Cross section (fb)
$t\bar{t} \ h$	4.3623
$t\bar{t} \ /h$	5.2391
$Z'(m_{Z'} = 150\text{GeV})$	0.33319
$Z'(m_{Z'} = 200\text{GeV})$	0.282
$Z'(m_{Z'} = 250\text{GeV})$	0.167
$Z'(m_{Z'} = 300\text{GeV})$	0.133
$Z'(m_{Z'} = 350\text{GeV})$	0.108
$Z'(m_{Z'} = 1000\text{GeV})$	0.0134
$Z'(m_{Z'} = 1500\text{GeV})$	0.0040678
$Z'(m_{Z'} = 2000\text{GeV})$	0.00091233

4.2 MadAnalysis

FALTAAA

The unweighted events files obtained with MadGraph contain the information of the process that we will further analyze. These files are read and processed using MadAnalysis, a framework for phenomenological investigations at particle colliders based on C++ [48], from which histograms of the production of different distributions can be obtained. For the study of the Z' production all the data obtained will be used to generate histograms for the analysis of mass distributions, cross section and other important parameters of the experiment that will allow us to study the data of the simulated events.

4.3 MadAnalysis expert mode

The data analysis, which involves the definition of the event selection criteria, selection of relevant topological distributions, study of efficiencies, etc, were performed using MadAnalysis expert mode. This program allows to process data using ROOT programming, an object-oriented C++ framework for data processing created by the European Organization for Nuclear Research (CERN) [49]. With the use of MadAnalysis in expert mode we were capable of performing all the cuts mentioned in Chapter 6.3 used to discriminate the signal from the backgrounds. For the semileptonic channel and the fully hadronic channel the final state jets and b-quarks were classified into three categories which are "Not Merged", "Partially Merged" and "Fully Merged", in order to distinguish the event production of FatJets (2-jet FatJet or 2-jet-b Fatjet), for the W boson and top quark reconstruction. Different selection parameters were also applied in order to make this reconstruction more accurate, the detailed analysis process performed is shown in Chapters ?? and ?. All the code used to classification, selection criteria implementation and generation of all the result presented in this document can be found in GITHUB. FALTA

5 Collider physics and experimental parameters

5.1 The Large Hadron Collider

The LHC at CERN is a 27 km two-ring-superconducting-hadron accelerator and collider installed in the Large Electron-Positron (LEP) collider tunnel, located approximately 100 m underground. Being a particle-particle collider, there are two rings with counter-rotating beams which collide at the detectors locations (these detectors and its characteristics are mentioned in Chapter 5.1.1) [50]. The main detectors of the LHC are CMS, ATLAS, ALICE and LHCb which are shown in Figure 10. In total the LHC has 1232 superconducting dipole magnets which provide a ~ 8 T magnetic field for bending charged particle's (such as protons or heavy ions) trajectories and 392 main quadrupole magnets, which help to keep the bunches in a compact beam with four magnetic poles arranged symmetrically around the beam pipe to squeeze the beam either horizontally or vertically [50][51]. Although the LHC accelerates heavy ions and protons, this study is focused only on proton-proton collision processes and on the detection of generated particles via these collisions.

The beams that enter the LHC are prepared at the CERN injector complex, shown in Figure 10, which comprises several accelerators, linacs, booster, Proton Synchrotron, and finally the Super Proton Synchrotron (SPS). In the SPS the beam is accelerated to the LHC injection energy of 450 GeV and then transferred via about 3 km long transfer lines to the LHC [52].

The main motivation of the LHC was to explain the nature of EW symmetry breaking and the Higgs mechanism. Currently, the aim of the LHC is to reveal physics beyond the SM with centre of mass collision energies of up to $\sqrt{s} = 14$ TeV. [IOP1] The number of events per second generated in the LHC collisions is given by

$$N_{\text{event}} = \frac{dR}{dt} = L\sigma_{\text{event}}, \quad (5.1)$$

where σ_{event} is the cross section for the event, L the machine luminosity and N_{event} the number of events per second. This luminosity is a parameter that measures the ability of a particle accelerator to produce a required number of interactions, i.e. it provides information about our accelerators' specifications and its performance and it depends only on the beam parameters as:

$$L = \frac{N_1 N_2 n_b f_{\text{rev}}}{4\pi\sigma_1\sigma_2} F,$$

where n_b is the number of bunches per beam, $N_1 N_2$ the number of particles per bunch

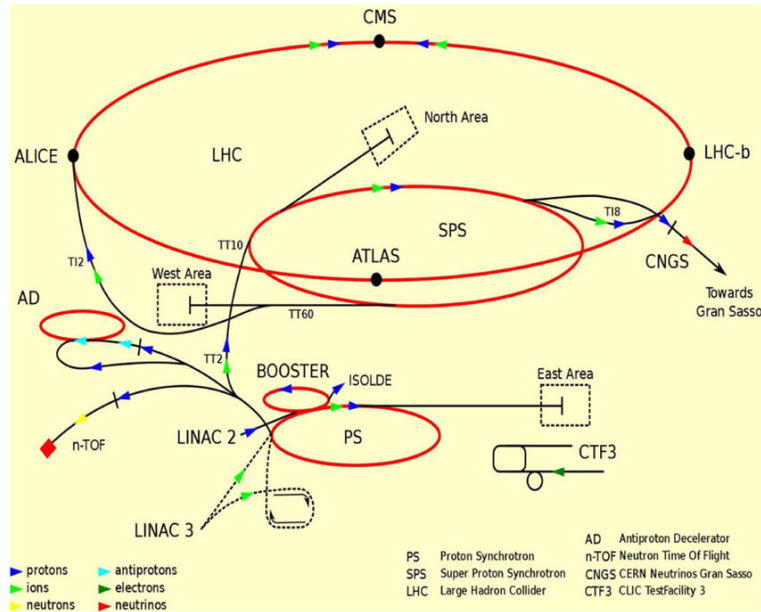


Figure 10: Scheme of the injector complex at CERN for beams to finally enter the LHC [52]

in each bunch, f_{rev} the revolution frequency, $4\pi\sigma_1\sigma_2$ the effective interaction area, and F the geometric luminosity reduction factor due to the crossing angle at the interaction point [53] [54].

From the definition of luminosity used one can also define an integrated luminosity as

$$L_{\text{int}} = \int_{t_1}^{t_2} L dt; \quad (5.2)$$

This parameter is important as the larger the integrated luminosity, the larger the data set which enables the study of physics beyond the SM and precision measurements of rare processes [50]. At full design luminosity each of the two beams colliding will contain 2,808 bunches of 1.15×10^{11} protons and the interval between crossings is 25 ns.

5.1.1 Detectors

As mentioned earlier the main detectors of the LHC are ALICE, ATLAS, LHCb and CMS. The ALICE (A Large Ion Collider Experiment) is a detector dedicated to heavy-ion physics, then it is used to study strongly interacting matter at high energy densities created at proton–proton, proton–nucleus and nucleus–nucleus collisions. It is also a great detector to study some aspects of QCD, such as diffraction and photon-induced interactions [55], and its Inner Tracking System (ITS), consists of six cylindrical layers of silicon detectors with three different technologies; two layers of pixel detectors, two layers each of drift, and strip detectors [55].

The ATLAS (A Toroidal LHC ApparatuS) detector has the same scientific goals as the CMS experiment, which is explained with great detail in Section 5.1.1.1, as the simulations generated in this phenomenological study are based on the CMS detector, its geometry, acceptance and efficiencies. The ATLAS detector is then very similar to CMS but it differs from it as it uses different technical solutions and a different magnet-system design. On the other hand, the LHCb (The Large Hadron Collider beauty) is an experiment designed for the study of b-hadron and c-hadron decays, using proton-proton collisions, it specializes in investigating the slight differences between matter and antimatter through the study of these hadrons. This detector uses a series of subdetectors to detect mainly forward particles, covering pseudorapidities in the range of $2 < \eta < 5$, unlike CMS or ATLAS which surrounds the entire collision point with enclosed detectors. The LHCb includes a high-precision tracking system consisting of a silicon-strip vertex detector, a large-area silicon-strip detector located upstream of a dipole magnet and three stations of silicon-strip detectors and straw drift tubes placed downstream of the magnet [56].

5.1.1.1 CMS

The Compact Muon Solenoid (CMS) detector is a multi-purpose apparatus due to operate at the LHC at CERN, the detector requirements to meet the goals of the LHC are related to its reconstruction efficiency, good particle identification and a good momentum resolution. For these, the main distinguishing features of CMS (shown in Figure 11) are a high-field solenoid, a full-silicon-based inner tracking system, and a homogeneous scintillating-crystals-based electromagnetic calorimeter, which all are designed to meet all the detector requirements [57] [58].

The tracker

One important parameter to study the nature of our collisions is the momentum of the particles. One method to calculate the momentum of a particle is to track its path through a magnetic field, because the path of the particles tells us about its momentum: the more curved the path, the less momentum the particle had. The tracking system at CMS is formed by the pixel detector and the silicon strips. The tracker in the CMS detector is designed to make precise and efficient measurements of the trajectories of charged particles emerging from the collision along with a precise reconstruction of secondary vertices. The precision tracking detectors cover the region $|\eta| < 2.5$. The tracker can reconstruct the paths of muons, electrons and hadrons and also record the paths coming from the decay of very short-lived particles [57].

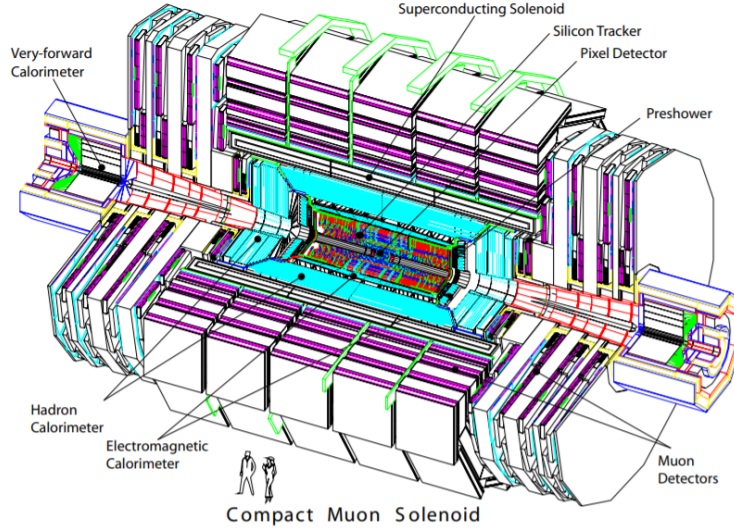


Figure 11: Caption [57]

Electromagnetic (ECAL) and hadronic calorimeters (HCAL)

The electromagnetic calorimeter (ECAL) is a homogeneous calorimeter, it forms a layer between the tracker and the HCAL and it is designed to measure the energies of electrons and photons with high precision, it is made of lead tungstate (PbWO_4) crystals, an optical clear material ideal for stopping the high energy particles. These crystals produce well defined photon proportional to the particle's energy. The hadronic calorimeters on the other hand are important for the measurement of hadrons, for example protons, neutrons, pions and kaons, and neutrinos or exotic particles resulting in apparent missing transverse energy [57].

Solenoid magnet and muon detector system

Outside of the tracking system and the calorimeters the CMS has a 3.8 T large solenoid magnet which allows to determine the charge/mass ratio of particles from the curvature of the path that they follow under the presence of said magnetic field, and lastly because of its mass muons can penetrate all the previous layers of the detector without interacting at all with any of them, i.e. they are not stopped by any of the calorimeters and therefore there is a last layer of chambers that have three functions: muon identification, momentum measurement and triggering. To do the muon identification and measure its momentum there are three detectors used: drift tubes (DT), cathode strip chambers (CSC) and resistive plate chambers (RPC). All the muon detector elements cover the pseudorapidity interval $|\eta| < 2.4$ and so muon identification is ensured over the range corresponding to $10^\circ < \theta < 170^\circ$ [57].

The coordinate system adopted by CMS has the origin centered at the collision point,

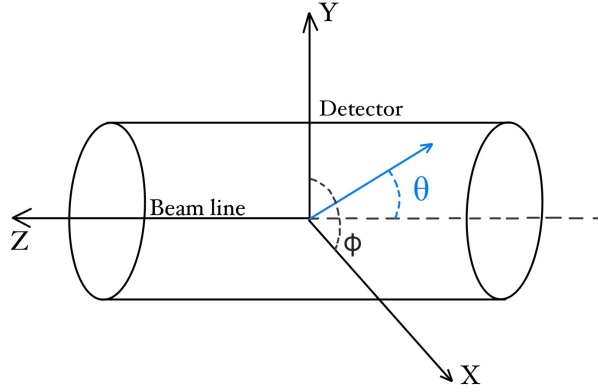


Figure 12: Caption

where the z -axis points along the beam direction, the y -axis pointing vertically upward, and the x -axis pointing radially inward toward the center of the LHC as shown in Figure 12. The azimuthal angle ϕ , the polar angle θ and other topological variables are explained in the following Chapter (5.2) [57].

5.2 Experimental parameters: Kinematic and topological variables of the signal

5.2.1 Pseudorapidity and azimuthal angle

The pseudorapidity denoted η and the azimuthal angle ϕ are measurements related to the angles at which the final particles are produced. The parameter η corresponds to the spatial coordinate involving the angle that the resulting particle forms with the beam axis, and it is defined as

$$\eta = -\ln \left(\tan \left(\frac{\theta}{2} \right) \right), \quad (5.3)$$

where θ is the polar angle, the angle between the momentum of the particle and the z axis, which is the direction of the beam. On the other hand, ϕ corresponds to the angle formed by the momentum of the particle in the XY plane, the transverse plane.

5.2.2 Transverse momentum

As the final particles travel mostly in the XY plane it is important to study the behavior of the transverse momentum denoted p_T which is the component of the momentum in the perpendicular plane i.e.

$$p_T = p \sin(\theta) = \frac{p}{\cosh(\eta)} = \sqrt{p_x^2 + p_y^2} \quad (5.4)$$

5.2.3 Angular distance

Another important spacial measurement corresponds to the angular distance δR defined as

$$\Delta R = \sqrt{(\Delta\eta)^2 + (\Delta\phi)^2}, \quad (5.5)$$

this angular distance between two objects corresponds to the separation between them in the $\eta\phi$ space in which the direction of an outgoing particle is represented as a point in this plane and consequently a small δR means that the particles travel in the same direction. If the behaviors of the distributions show peaks near a value of π means that the final particles travel in opposite directions.

6 Phenomenological analysis

6.1 Preliminary analysis

For the first analysis of the data obtained, as mentioned in Chapter 4.1, some distributions were observed for the fully-hadronic channel shown in Figure 8b and its results are shown in this Chapter. It is included a cross section study, analysis of kinematic and topological variables for the final particles ($\tau^+ \tau^-$) coming from the Z' , and histograms of kinematic and topological variables of the signal and two dominant backgrounds.

Further work, developed in the following chapters, include a detailed analysis using MadAnalysis expert mode, where the event selection criteria is defined, and the corresponding data analysis is performed using C++ coding.

Cross Section: A graph of the signal cross section as function of the Z' boson mass is shown in Figure 13. In this plot it is also shown how the cross section changes based on how strong is the coupling of the Z' boson to the light and heavy SM fermions. The behavior of the distribution demonstrate that the larger the mass or the lower the coupling constants are, the less probable our interaction becomes i.e. smaller $M_{Z'}$ and higher coupling to SM fermions give us more probable decays.

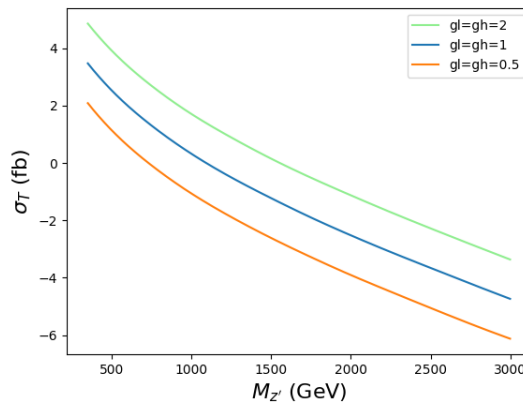
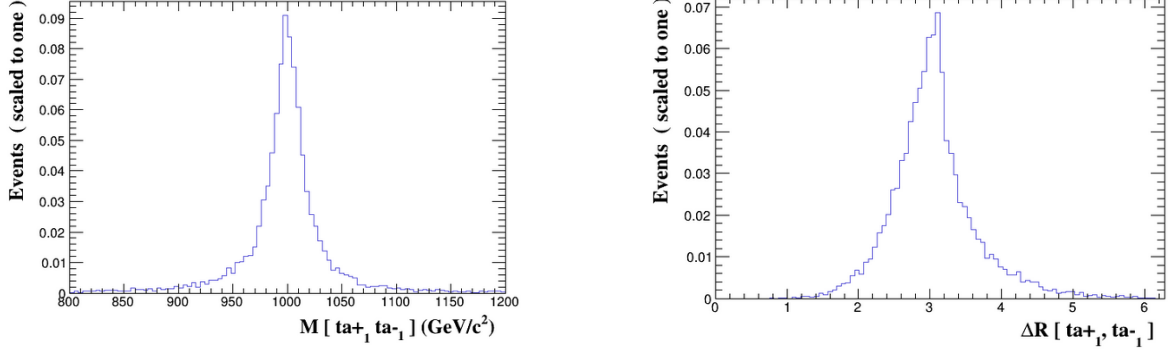


Figure 13: Cross section vs Z' mass in a logarithmic scale, for different light and heavy coupling constants of the Z' .

Reconstructed Mass: With the use of MadAnalysis the reconstructed mass obtained from the tau leptons from the Z' boson decay is shown in Figure 14a. As one can see from the figure the mass of the Z' was obtained with a peak at 1000 GeV, corresponding to the mass set at the configuration cards in the model used for this analysis.



(a) Reconstructed mass of the Z' boson using the final particles: $\tau^+ \tau^-$ with higher p_T .

(b) Distribution of angular distance between leading p_T τ particles.

Figure 14: Reconstructed masses and angular distribution of the final particles $\tau^+ \tau^-$ with Z' as a mother particle.

Angular distance: Figure 14b shows the angular distance between τ particles that come from the Z' generated in the process. The behavior of the distributions shows a peak near a value of π which means that our particles travel in opposite directions as expected from the theory.

Transverse momentum: Figure 15 shows the values of p_T obtained for the particles produced from the Z' . The peak of the distribution lies around 500 GeV, for both particles as expected from energy conservation, because τ^+ and τ^- would have very low P_z momentum and both presented peaks of transverse momentum which sum up to ~ 1000 GeV, this adds up well to the initial energy $\sim M_{Z'}$.

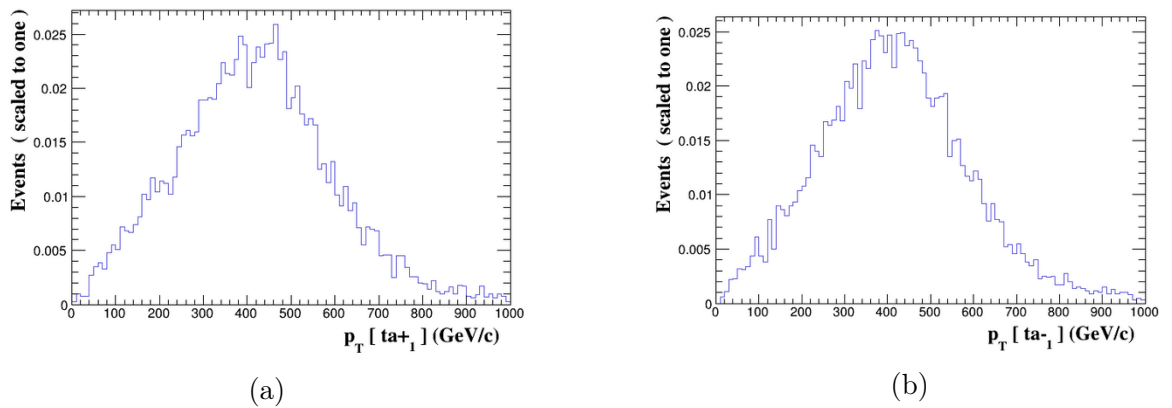


Figure 15: Distribution of the transverse momentum p_T of the final τ^+ (15a) and τ^- (15b) leptons.

Pseudorapidity and azimuthal angle: Figure 16 shows the distributions obtained when looking at the η parameter for the leading order τ particles (i.e. the final τ particles with higher p_T rank).

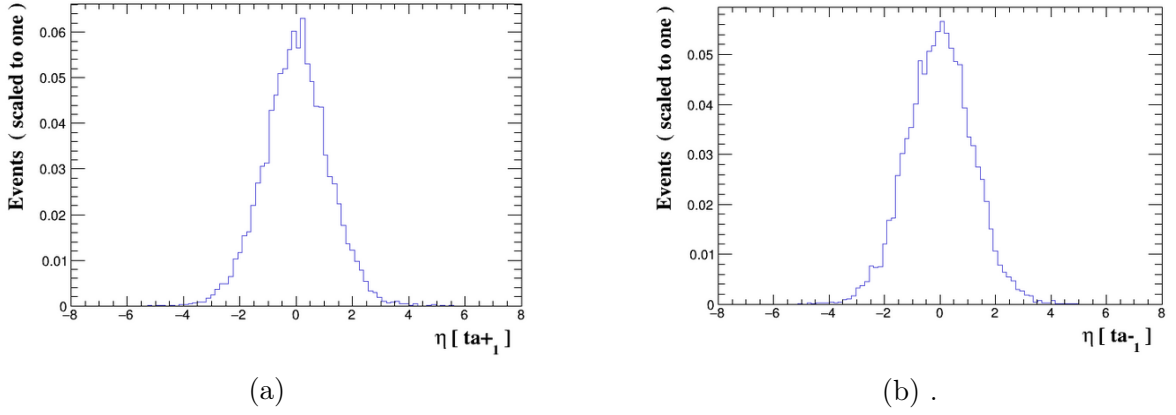


Figure 16: Distribution of pseudorapidity for the τ^+ (16a) and τ^- (16b) particles of higher rank in p_T .

The distribution obtained in Figure 16 shows that particles tend to be produced in the XY plane, perpendicular to the beam direction, meaning that particles carry very low momentum in the z direction as expected.

On the other hand, Figure 17 shows the lack of preference in the direction in the XY plane when looking at the ϕ parameter, which must be in fact aleatory.

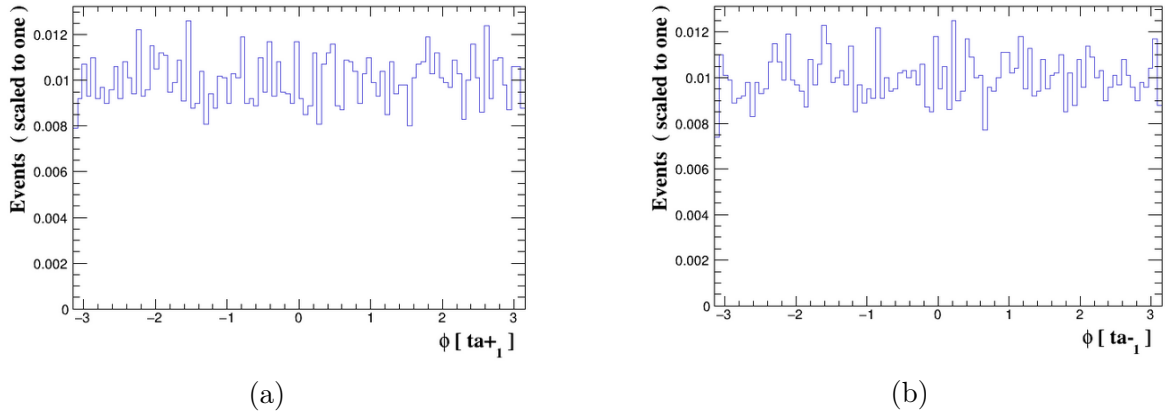


Figure 17: Distribution of azimuthal angle for the τ^+ (17a) and τ^- (17b) particles of higher rank in p_T .

According to Figure 14b both particles result in opposite position with a separation in the η - ϕ plane of π . This can be also observed by looking at the difference between the azimuthal angles of both particles, due to the fact that both τ^+ and τ^- have a pseudorapidity of ~ 0 .

The results of looking at the $\delta\phi$ of the τ particles is shown in Figure 18 which shows that the difference in the azimuthal angle corresponds to π or $-\pi$ as expected from the behavior of the angular distance.

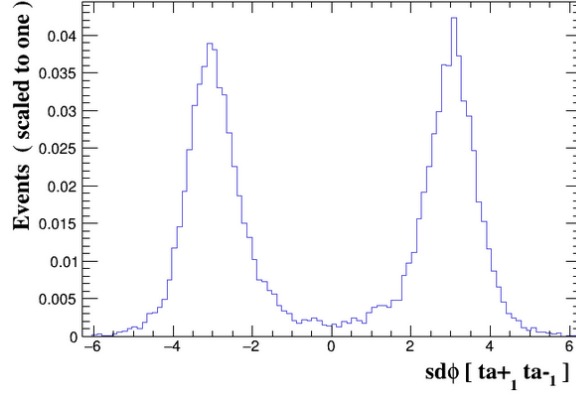


Figure 18: Difference of the azimuthal angle ϕ for the final τ leptons.

6.2 Event classification

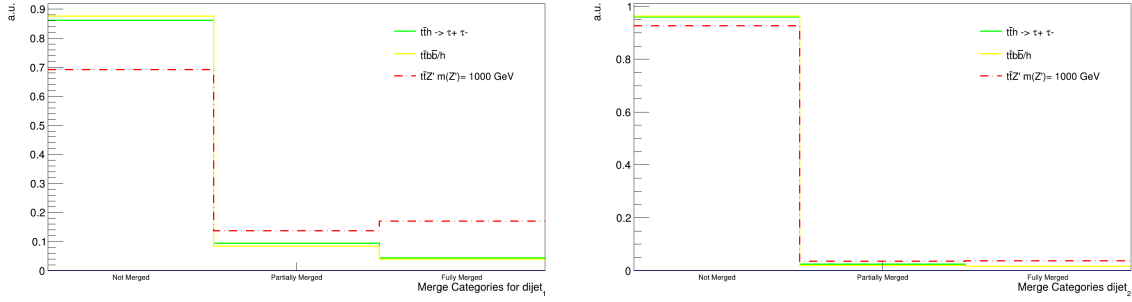
For both channels, semileptonic and fully hadronic, all the events produced were categorized into three different groups, depending on the angular distance ΔR of the jet pairs and the b -quark, as defined in 5.5. The categories are:

- **Not merged:** Events that fall into this category have two final state jets coming from the W boson that are very far apart, i.e. $\Delta R(j_1, j_2) > 0.8$.

If jets have a $\Delta R(j_1, j_2) < 0.8$ the event is classified as **Merged** which is divided into two categories:

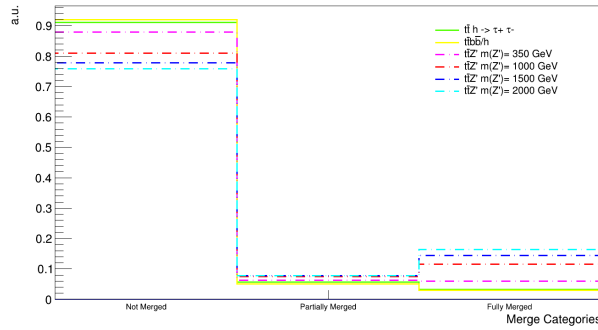
- **Partially merged:** The events have final state jets with a $\Delta R(j_1, j_2) < 0.8$ which allows us to reconstruct a dijet, a single object which satisfies ($p_{\text{dijet}} = p_{j_1} + p_{j_2}$), since experimentally because of the closeness of the two jets, they are observed as one fat-jet. In this case also the reconstructed dijet is produced distant from the b -quark, with a $\Delta R(j_1 j_2, b\text{-quark}) > 1.0$ between the dijet and the b -quark.
- **Fully merged:** Case in which we can also reconstruct a dijet ($\Delta R(j_1, j_2) < 0.8$) as a single object and also the b -quark is close enough ($\Delta R(j_1 j_2, b\text{-quark}) < 1.0$) that the three final state particles are observed experimentally as a single Fat-Jet.

In order to choose correctly the pair of jets and the b -quark associated with each pair, different procedures were used depending on whether the channel is fully hadronic or semileptonic, both cases are explained in more detail in Chapter (6.3). In general for the semi-leptonic and the fully-hadronic channels the distribution of events classified into these three categories is shown in Figure 19, where we can see that in both cases the majority of the events classify as Not Merged. In the fully-hadronic channel, showed in Figures 19a and 19b, the pairs were Not Merged 62.9% of the times and 92.6% of the times respectively. For the semi-leptonic channel, where we only have one (b - quark, dijet) pair, the range



(a) Percentage of times the first b – *quark dijet* pair is classified as Not Merged, Partially Merged and Fully Merged.

(b) Percentage of times the second b – *quark dijet* pair is classified as Not Merged, Partially Merged and Fully Merged.



(c) Percentage of times the b – *quark dijet* pair is classified as Not Merged, Partially Merged and Fully Merged.

Figure 19: Figures (a), (b) and (c) show how often a pair of b – *quark dijet* was categorized as Not Merged, Partially Merged or Fully Merged, where (a) and (b) correspond to both pair of jets of the fully-hadronic channel and (c) corresponds to the semi-leptonic channel

of events that classified as Not Merged is between 75% and 90% for the different signals. From now on, all plots with y – *axis* = *a.u.* corresponds to number of events scaled to one, i.e. the integral over all the histogram is 1, this normalization is made due to the fact that the number of events for the signals is different to the number of events of the backgrounds, as mentioned in Chapter 4.1.

6.3 Selection criteria

6.3.1 Fully hadronic channel

For the fully hadronic channel the goal was to reconstruct accurately the two top quarks producing final states of b –*quark* and two jets. Due to the nature of the process the final states, as shown in Figure 8a, have in total 4 jets and 2 b –*quarks* which we would like to differentiate, i.e. be capable of discriminate which set of b –*quarks* and jets came from which top quark. There are six possible ways of combining all the final states, as shown

in Figure 20, so with the use of MadAnalysis expert mode, for each event of the process, we made a loop over all possible combinations and established some selection criteria in order to get the correct pairs. Jets are classified according to their p_T rank (i.e. j_1 is the jet with highest p_T and j_4 the one with lowest p_T), the loops over all possible pairs were performed such that the pair 1 of jets is formed by j_1 and whichever other jet classified as its partner, as shown in Figure 20, and pair 2 is formed with the remaining jets.

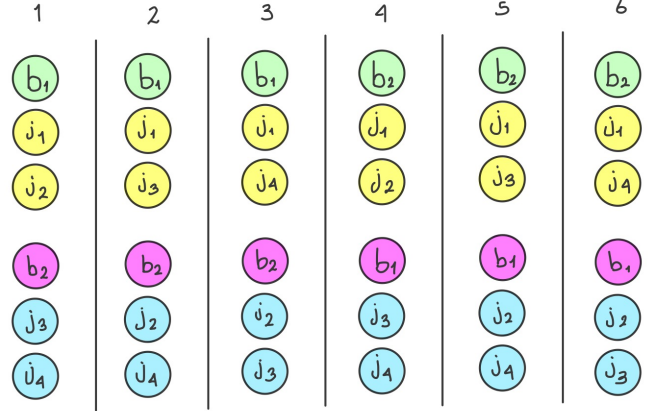


Figure 20: Graphic representation of all the possible six combinations of all the final state b – quarks and jets that can be formed in the fully hadronic channel.

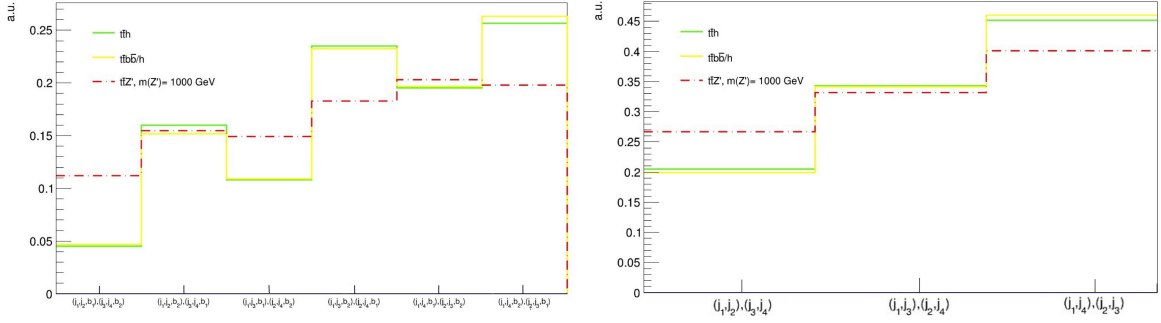
The first selection criteria used for the analysis was based on the reconstructed mass of the jets, and we will call it the "Relative mass difference" criteria. For this, on each event generated, a loop over all jets (non b -jets) was performed, then we selected which pair of jets ($j_i j_k$) had a reconstructed mass that minimized its relative difference with the M_W PDG value (80.379 ± 0.012 GeV) using equation 6.1

$$\epsilon_1 = \frac{|M_1 - M_W|}{M_W}, \quad \epsilon_2 = \frac{|M_2 - M_W|}{M_W}, \quad (6.1)$$

where ϵ_1 is the difference obtained with the first pair with indexes j_1, j_{index_2} of jets and ϵ_2 with the second pair with indexes j_{index_3}, j_{index_4} , which is given once we chose the first one, as seen in Figure 20. Now we define $\epsilon = \epsilon_1 + \epsilon_2$ and the selected pairs that are said to reduce the mass difference are the ones that presented the smallest value of ϵ .

After our pairs of jets have been ruled out by this first criteria, a second criteria was implemented when the two jets classified as Not Merged. This criteria consisted of checking the charge of the particles and we will call it "Charge criteria". In this step it was verified that the charge of the pair of jets sum up to ± 1 :

$$Q_{j_1} + Q_{j_{index_2}} = \pm 1 \quad \text{or (and)} \quad Q_{j_{index_3}} + Q_{j_{index_4}} = \pm 1. \quad (6.2)$$



(a) The histogram shows how many time each pair of b -quark and two jets was chosen as the respective pairs coming from a top quark after applying the selection criteria.

(b) The histogram shows how many time each pair of jets coming from the $W^+ W^-$ was chosen as the correct pair after applying the selection criteria mentioned.

Figure 21: Distributions of the selected pairs that reconstruct correctly the W boson and the top quarks according to the selection criteria established.

This is the expected value due to the fact that if two jets were produced in the same vertex, because of charge conservation, its charge must sum up to the W^\pm charge. Although the charge criteria is not used in the Fully Merged and the Partially Merged categories, it is used 69.2% and 92.6% of the times for the two pair of jets, as that is the percentage of events that classified as Not Merged.

Once the two pairs of jets were selected using these criteria, the "Relative mass difference" criteria was used once again, this time for the top quark reconstruction, so that the two b -quarks were distributed to the two pairs of jets in such a way that the corresponding ϵ was minimized. With those first two selection criteria applied to the jet pairs and the mass criteria for the selections of the pair of b -quark and two jets, histograms of the frequency in which a certain pair j_i, j_k (or $j_i j_k$, b -quark) was chosen as the correct pair coming from a W boson (or a top quark) were plotted and are shown in Figure 21

As shown in Figure 21 there seems to be no prevailing preference for neither pairs of jets nor pairs of b -quark and two jets. Because of this, a check-up in order to determine the efficiency of the selection criteria was used. It consisted of asking for the mother particle of the final states particles and confirm that j_1 and j_{index_2} (j_{index_3} and j_{index_4}) had the same mother particle. Although, when working with non-simulated data it is not possible to check the mother particles, we used this method just for reference as how efficient the selection criteria turned out to be with the simulations, giving us a hint of the feasibility of the selection criteria used. The implementation of this check-up method consisted of finding the mother particle of j_1 and j_{index_2} (or j_{index_3} and j_{index_4}) comparing them to see if they were equal, and then, checking that j_1 and j_{index_2} had a different

mother particle than j_{index_3} and j_{index_4} . This was done in order to corroborate that the method was capable of distinguishing between both particles W^+ and W^- , if at the end both conditions are true the pairs are classified as "Correct mother particle", otherwise they are classified as "Not correct mother particle", the distribution of how many times the selected pair of jets satisfied this check-up is presented in Figure 22.

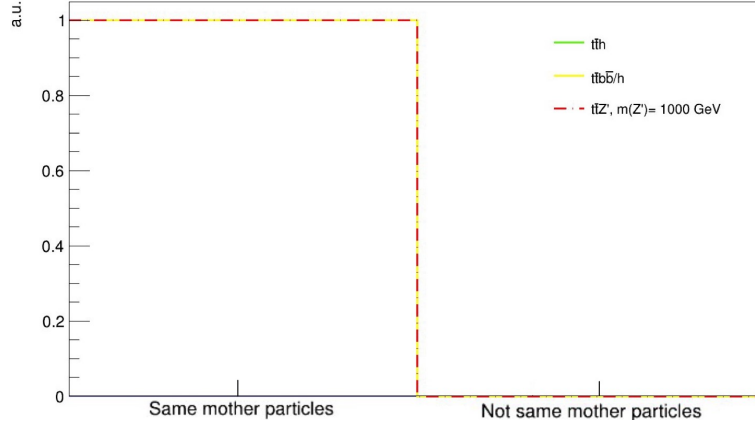


Figure 22: Distribution of how many times the two jets of the selected pair j_1 and j_{index_2} (j_{index_3} and j_{index_4}) did have the same mother particle.

From the distribution obtained we were capable of distinguish the amount of events which did not reconstruct correctly the W boson, it corresponded to 90 out of 1 million events, i.e. the selecting pairs criteria for the jets is 99.991 % effective.

Different extra selection criteria were applied to check if there were any changes in the behavior of the selected pairs when changing the criteria used to identify the correct pair of jets that reconstructed the W boson. We established a cut in the ΔR such that the two jets had a ΔR smaller than 2 or 3 after the applying the "Relative mass difference" and the "Charge criteria". Also, a cut only with the "Relative mass difference" and the $\Delta R < 2$ criteria, and one with just the "Relative mass difference" and no "Charge criteria" were checked too. As one can see from Figure 23 the behavior of the selected pairs did not change but rather a decrease in the amount of data was obtained, therefore, we concluded that these extra cuts on the ΔR of the pairs of jets (j_i, j_k) did not contribute to the pair selection but excluded events from the analysis.

Finally, for the selected pairs of jets (j_i, j_k) and pairs of *b-quark* and two jets, it was found that in the majority of the events (63% and 75% of the time respectively), both chosen pairs were the ones with smallest ΔR of all possible pairs, as shown in Figures 24a and 24b.

All these plots presented on this Chapter were made in order to analyse the distribution

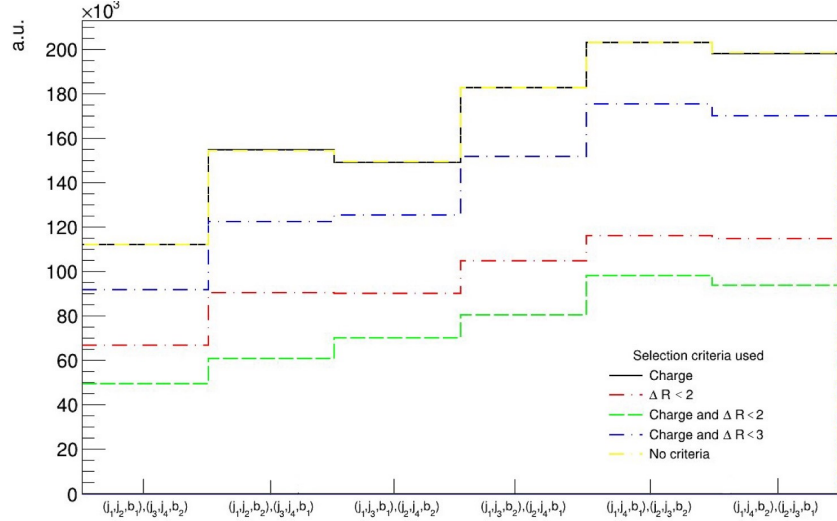
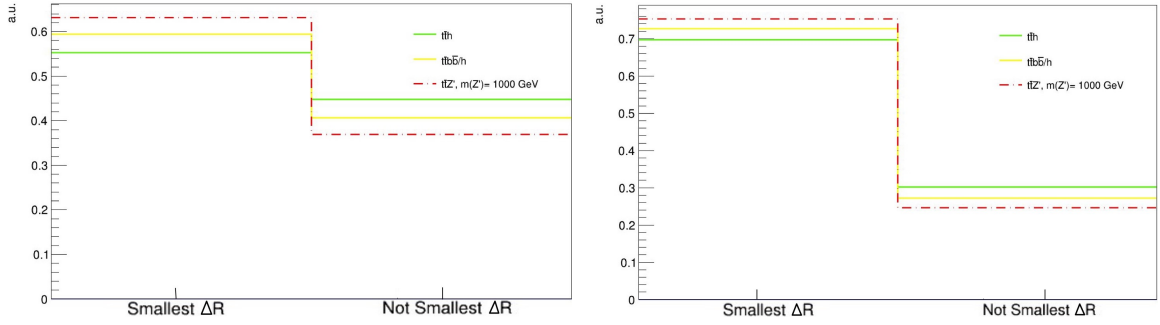


Figure 23: Distribution of the selected pair under different extreme selection criteria after using the "Reconstructed mass" criteria.



(a) The histogram shows how many time each pair of two jets chosen as the selected pair was also the pair of jets with the smallest ΔR after applying the selection criteria.

(b) The histogram shows how many time each pair of b -quark and two jets was chosen as the selected pair also corresponded to the pair of jets with the smallest ΔR .

Figure 24: Distributions of the frequency in which the selected pair (Figure (a) for jets and (b) for b -quark and jets) corresponded also to the pair that presented the smallest value of $\Delta R(j_i, j_k)$ and $\Delta R(j_i j_k, b\text{-quark})$ respectively.

of selected pairs using the selection criteria explained above, the topological behavior of the pairs of jets selected (j_i, j_k) and the efficiency of the method used. Nonetheless, due to the intrinsic complexity of the channel (observed in non-preference of a certain pair of particles in the top and W reconstructions) a more in detail study with the use of machine learning techniques is suggested to be performed.

6.3.2 Semi-leptonic channel

The semi-leptonic channel studied corresponds to the process presented in Figure 8a, in which the final states correspond to two jets (j_1 and j_2) and a l, ν_l coming from one of the W^\pm bosons, two b -quarks, and two leptons (τ^+, τ^-) coming from the Z' boson. The

goal of this study is to find which criteria allow us to differentiate the signal from the SM backgrounds that present bigger cross sections, and consequently limit the possible measurement of the signal (i.e. the Z' production). This phenomenological analysis was performed with the study of various kinematic and topological variables of the signal and backgrounds.

As in Chapter 6.1, all the distributions shown next, have been normalized to the unity in order to compare the shapes of the histograms for the signals and background samples, unless specified otherwise. The histograms shown in this subsection contain a set of distributions that describe the general behavior of the signal samples for the high mass classification.

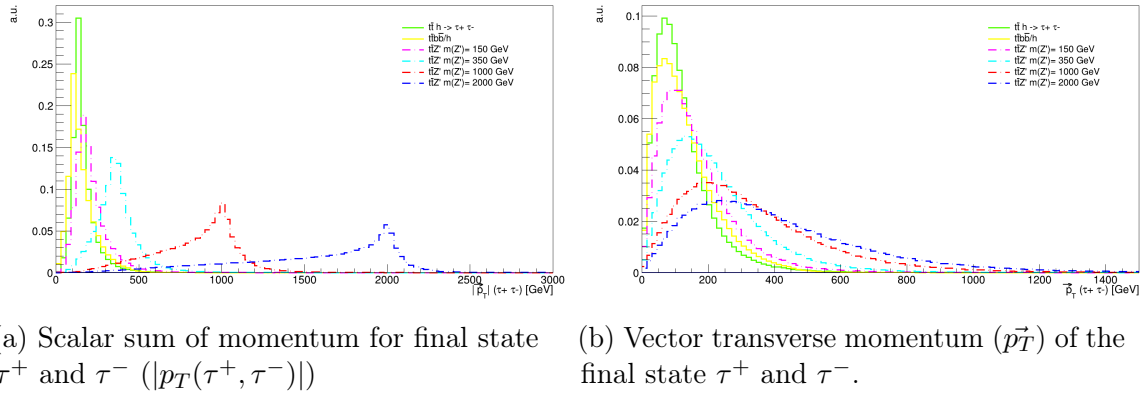


Figure 25: p_T distributions of the τ particles coming from the Z' (or Z , γ^* , higgs for the backgrounds considered) for four different values of $m_{Z'}$ and the two relevant backgrounds.

In Figure 25 it is observed that as one would expect, the scalar p_T distribution for the two taus have peaks around the theoretical mass of their mother particle, and therefore showing distributions shifted towards higher values for the high $m_{Z'}$ signals, unlike the backgrounds, in which the two taus are generated by lighter mediators.

From Figure 26 it can be seen that since the production of the two taus does not depend on the azimuthal angle (ϕ), as expected there is no preference in its distribution. Figure 26 shows the result only for the highest p_T τ , as a similar result was obtained for the other τ .

The difference in the azimuth angle ($\delta\phi$) between the two taus coming from the $t \bar{t}$ annihilation is shown in Figure 27. It can be observed that the heavier the mediator that produces the two taus, the graph shows a shifting of the maximum value towards $\pm\pi$. This is due to the fact that in the case of higher masses of the Z' , we can consider $p_T \approx 0$. Therefore, the two taus are expected to be produced back to back, meaning that $\delta\phi \approx \pm\pi$.

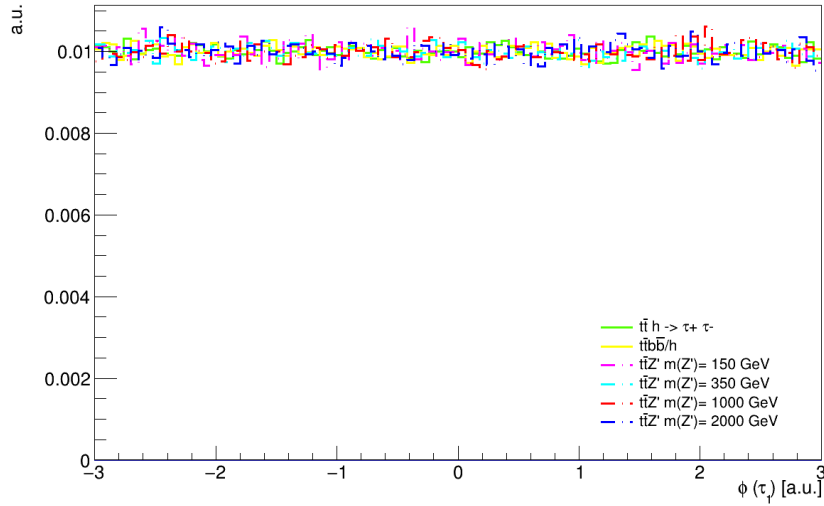


Figure 26: Distribution of the azimuthal angle ϕ for the final state τ of higher p_T .

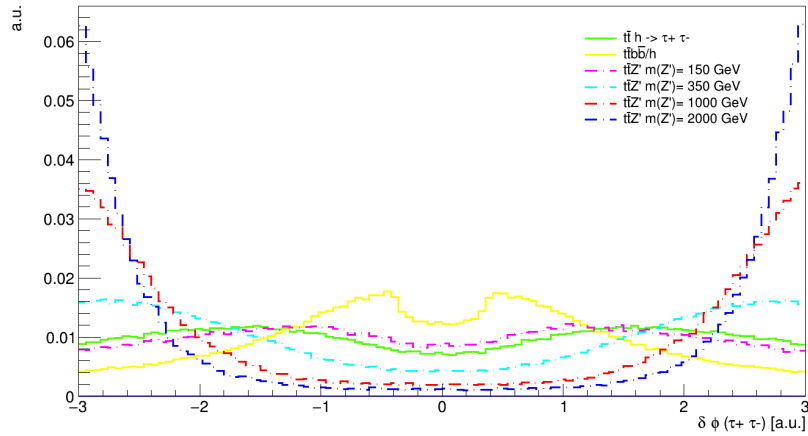


Figure 27: Distribution of difference on the azimuthal angle ϕ between the final state τ leptons coming from the Z' .

The main criteria used to perform cuts was the transverse momentum (p_T) and the pseudorapidity ($|\eta|$) of the different final state particles. These cuts were mainly applied to fulfill the requirements of the CMS and ATLAS detectors explained in Chapter 5.1.1.1 due to experimental limitations, and also to distinguish $t \bar{t}$ channels at the LCH from all other possible processes generated. The selection criteria used for both high mass signals and low mass signals is shown in Table 4.

In Table 4, Cut 2 and 3 are specific for the Not Merged classification since this is the only one with final states $j_1, j_2, b\text{-quark}_1$ and $b\text{-quark}_2$, due to the fact that physically they are produced far apart from each other so that they can be distinguished experimentally. For the Partially Merged case one of these two criteria changes in order to fit the actual final state particles obtained, and the changes are shown in Table 5.

Table 4: Initial event selection criteria used for background reduction.

# Cut	used criteria	Particles	Selection
1	$\vec{p}_T; \eta $	$e^\pm (\mu^\pm)$ coming from W boson	$\vec{p}_T > 35$ GeV and $ \eta < 2.4$
2	$\vec{p}_T; \eta $	j_1 and j_2	$\vec{p}_T > 30$ GeV and $ \eta < 5$
3	$\vec{p}_T; \eta $	$b\text{-quark}_1$ and $b\text{-quark}_2$	$\vec{p}_T > 30$ GeV and $ \eta < 2.4$
4	E^{miss}	-	$E^{miss} > 30$ GeV
5	$\vec{p}_T; \eta ; Q$	τ^+ and τ^-	$\vec{p}_T > 20$ GeV, $ \eta < 2.4$ and $Q(\tau^+)Q(\tau^-) < 1$

Table 5: Modified event selection criteria for the Partially merged case.

# Cut	used criteria	Particles	Selection
2	$\vec{p}_T; \eta $	j (fat-jet) coming from W boson	$\vec{p}_T > 30$ GeV and $ \eta < 5$

The parameter used for the selection is the same but now we only have one jet, since, as explained earlier, because of the closeness of the two jets resulting from the W boson, the jets (j_1 and j_2) are detected as a single object (a fat-jet) in the Partially Merged category. Lastly, for the Fully Merged case, both the two jets (j_1, j_2) and one of the two $b\text{-quarks}$ are detected as a single fat-jet, and so, cuts 2 and 3 change to the ones presented in Table 6.

Table 6: Modified event selection criteria for the Fully merged case.

# Cut	used criteria	Particles	Selection
2	$\vec{p}_T; \eta $	j (Fat-jet) coming from W boson	$\vec{p}_T > 30$ GeV and $ \eta < 5$
3	$\vec{p}_T; \eta $	$b\text{-quark}$	$\vec{p}_T > 30$ GeV and $ \eta < 2.4$

The 3rd cut in this case checks the criteria for the respective $b\text{-quark}$ that was not used for the fat-jet formed with the two jets (j_1, j_2), i.e. the $b\text{-quark}$ coming from the same top quark as the W that is decaying into l, ν_l . The topological variable ΔR was used in order to determine which $b\text{-quark}$ was produced from the same top quark as the W decaying hadronically ($W^\pm \rightarrow j_1 j_2$). The selected $b\text{-quark}$ corresponded to that which minimized the ΔR between the $b\text{-quark}$ and the two jets (j_1, j_2) obtained in the channel, i.e. the $b\text{-quark}$ chosen was the one that satisfied $\min(\Delta R(b\text{-quark}_i, j_1 j_2))$.

The cuts showed in Tables 4, 5 and 6 were applied to each event run, and in the same order they are presented in the table. First, it was checked that there was at least one muon or electron which satisfied the criteria of Cut 1. Since we are studying the semi-leptonic channel, the only final state lepton (aside from the two taus coming from the Z') is the one coming from the W decay, which due to its low mass is expected to carry a p_T around half of the mass of the W boson. Then the second cut checked if there were exactly two jets (for Not Merged, and one jet for Partially and Fully Merged), the ones

coming from one of the two W bosons, which should have a p_T of around half of its mass and must have an $|\eta|$ smaller than 5 in order to fulfill the experimental constraints of the HCAL in the CMS experiment. The third cut checked there were exactly two *b-quarks* (for Not and Partially Merged, and only one *b-quark* for Fully Merged) that satisfied the used criteria, again to meet the limitations of the CMS detector. Fourth cut corresponds to the missing transverse energy, for which the selection value was chosen to be $E^{miss} > 30$ GeV. This value was calculated to be 10 GeV lesser than the expected E^{miss} value, which is approximately 40 GeV, half of the W^\pm mass. The 10 GeV threshold is used to make up for the experimental uncertainty in the measurement of the missing energy at the CMS and ATLAS detectors. The last cut applied was related to the leptons coming from the Z , Z' , γ^* or higgs, depending on the process being analyzed. This cut checked that there were two final τ leptons, that their momentum \vec{p} and its pseudorapidity η comply with the selection cuts and that the product of their charges is lesser than 1, since these leptons are expected to have opposite electric charge.

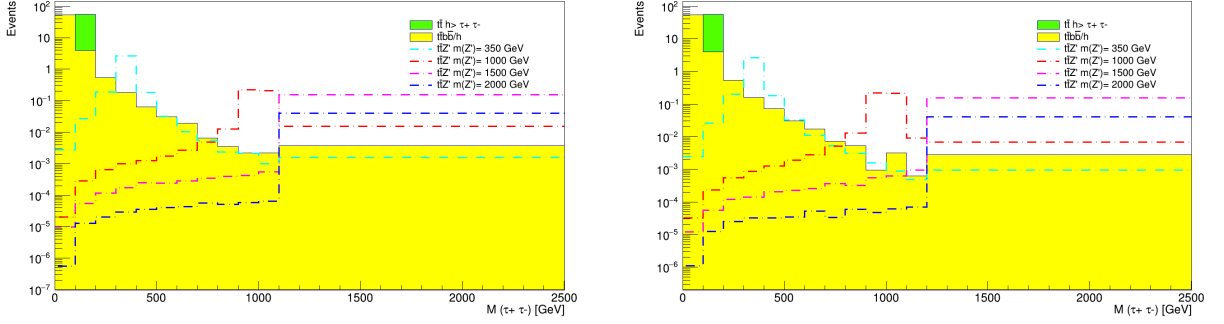
6.3.2.1 High mass classification

The semi-leptonic channel was studied separately for low masses and high masses as presented in Chapter 4.1. For high masses, after applying these 5 previously mentioned cuts to the all the signals and backgrounds, other extra two cuts were used, in order to reduce noise data and distinguish our signals. As one can see from Figure 25a due to the value of the masses that we are studying, a cut on the scalar p_T sum would allow to reduce the backgrounds significantly, and keep a high signal's data. Consequently, a scalar p_T cut was applied, i.e. the sixth cut for high masses of the Z' corresponded to requiring a minimum value in the scalar sum of p_T of the two τ particles of higher p_T , as they correspond to the only two produced in the channel. The cut applied is presented in Table 7:

Table 7: Sixth cut for high masses of the Z' for the Fully merged, partially merged and not merged categories.

# Cut	used criteria	Particles	Selection
6	$p_{T_1} + p_{T_2}$	τ^+ and τ^-	$p_{T_1} + p_{T_2} > 150$ GeV

The cut applied was low in order to keep enough statistics of the signals to study while ruling out a significant amount of background. Then, with the results obtained after applying these six cuts, a plot of the reconstructed mass of the two taus was used to determine the following cut, to further optimize the signal data over the backgrounds. The seventh cut applied to the signal corresponded then to a mass cut in which we checked at



(a) Stacked plot of reconstructed mass distribution for the semi-leptonic channel with $W^\pm \rightarrow e^\pm \nu_e(\bar{\nu}_e)$.

(b) Stacked plot of reconstructed mass distribution for the semi-leptonic channel with $W^\pm \rightarrow \mu^\pm \nu_\mu(\bar{\nu}_\mu)$.

Figure 28: Figures (a) and (b) show plots of the reconstructed mass of the two final state particles τ^+ and τ^- coming from the Z' (or Z , γ^* , higgs for the backgrounds considered) for the two channels studied of the decay of the W boson. These plots correspond to high mass signals ($m_{Z'} \geq 350$ GeV).

what value the signals exceeded the background number of events. This value corresponded to 290 GeV for both $W^\pm \rightarrow \mu^\pm \nu_\mu(\bar{\nu}_\mu)$ and $W^\pm \rightarrow e^\pm \nu_e(\bar{\nu}_e)$ as shown in Table 8.

Table 8: Seventh cut for high masses of the Z' for the Fully Merged, Partially Merged and Not Merged categories.

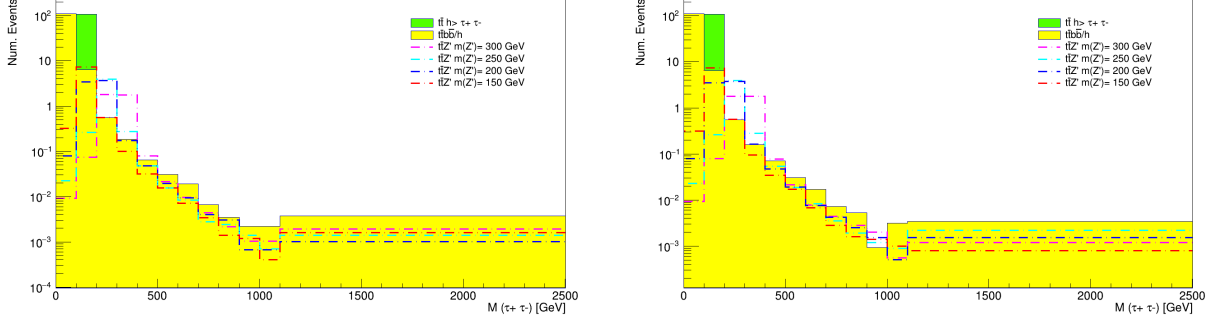
# Cut	used criteria	Particles	Selection
7	$m(\tau^+, \tau^-)$	τ^+ and τ^-	$m(\tau^+, \tau^-) > 290$ GeV

Here, and from now on, all plots will be made separately for the W boson decaying to first and second generation leptons. Before, we only presented a single plot either from the $W^\pm \rightarrow \mu^\pm \nu_\mu(\bar{\nu}_\mu)$ or $W^\pm \rightarrow e^\pm \nu_e(\bar{\nu}_e)$ without making a distinction between them since the behaviors observed were the same for both of them. The stacked plots were obtained for all the high mass signals and are presented in Figures 28a and 28b.

For the stacked plots the y - axis used was *Events*, which corresponds to the number of events normalized to the luminosity and cross section of each process, i.e.

$$Events = \frac{N_i}{N_0} \sigma \mathcal{L}, \quad (6.3)$$

where the value used for luminosity is $\mathcal{L} = 150 fb^{-1}$. On the grounds of the behaviour seen in Figures 28a and 28b, it is notable that signals with greater values of $m_{Z'}$ dominate over the total background. Last bin is an overflow bin from the value at which the statistics of the backgrounds are not enough due to the number of generated events, overflow goes from values 1100 GeV and 1200 GeV respectively for $W^\pm \rightarrow e^\pm \nu_e$ and $W^\pm \rightarrow \mu^\pm \nu_\mu$.



(a) Stacked plot of reconstructed mass distribution for the semi-leptonic channel with $W^\pm \rightarrow e^\pm \nu_e(\bar{\nu}_e)$.

(b) Stacked plot of reconstructed mass distribution for the semi-leptonic channel with $W^\pm \rightarrow \mu^\pm \nu_\mu(\bar{\nu}_\mu)$.

Figure 29: Figures (a) and (b) show plots of the reconstructed mass of the two final state particles τ^+ and τ^- coming from the Z' (or Z , γ^* , higgs for the backgrounds considered) for the two channels studied of the decay of the W boson. These plots correspond to low mass signals ($m_{Z'} \leq 350$ GeV).

The y – axis is adjusted to a logarithmic scale due to the differences of number of *Events* between backgrounds and signals, attributable to the cross sections of each event, presented in Table 3.

6.3.2.2 Low mass classification

As mentioned previously, masses of Z' with low values going from 150 GeV to 300 GeV were considered. The stacked plots of reconstructed mass, normalized to *Events*, for all the signals were obtained and are shown in Figures 29a and 29b. These plots are made using only five cuts, the ones presented in Table 4, because as seen in Figures 29a and 29b the distributions of these signals present peaks bordering on the peaks presented by the backgrounds. Hence, applying p_T or mass cuts would also suppress most of the signal data. For these low mass signals the dominant background, just like for high mass signals, corresponds to the $t\bar{t}$ process without Higgs, for which, for example, the lowest signal $t\bar{t} Z' m(Z') = 150$ GeV, cannot be distinguished from this background.

6.4 Efficiencies

In order to gauge how useful were the set of cuts applied to discriminate the signals from the backgrounds, the *Relative Efficiency* was implemented. This efficiency is defined as the ratio of the number of events that passed a certain cut vs the number of events before

that specific cut, so it is defined as:

$$\epsilon_i = \frac{N_i}{N_{i-1}} \pm \delta\epsilon_i, \quad \text{where: } \delta\epsilon_i = \epsilon_i \sqrt{\frac{1}{N_i} + \frac{1}{N_{i-1}}}. \quad (6.4)$$

Similarly, the cumulative efficiency is related to the total efficiency of all the applied cuts, thereby defined as

$$\epsilon_c = \prod_{i=1}^n \frac{N_i}{N_{i-1}} = \frac{N_n}{N_0}, \quad (6.5)$$

where n is the total number of cuts applied, and N_0 is the initial number of events without any cuts, taking into account the effect of all the cuts applied. Just like for the efficiency of a single cut, the cumulative efficiency has an uncertainty of $\delta\epsilon_c = \epsilon_c \sqrt{\frac{1}{N_n} + \frac{1}{N_0}}$. The efficiency of every cut and the cumulative efficiency for the high mass signals are presented in Table 9.

Table 9: Relative efficiencies for the signals and backgrounds of high mass processes for each cut applied, where the last column ϵ_c corresponds to the cumulative efficiency as defined in Equation 6.5. All efficiencies are expressed in percentages.

Efficiencies for $W \rightarrow e \nu_e$.								
Process	$\epsilon_1 (\times 100)$	$\epsilon_2 (\times 100)$	$\epsilon_3 (\times 100)$	$\epsilon_4 (\times 100)$	$\epsilon_5 (\times 100)$	$\epsilon_6 (\times 100)$	$\epsilon_7 (\times 100)$	$\epsilon_c (\times 100)$
$t\bar{t}h$	64.42 ± 0.14	54.13 ± 0.16	73.63 ± 0.27	73.17 ± 0.31	86.82 ± 0.41	52.21 ± 0.31	0	0
$t\bar{t}/h$	62.11 ± 0.14	53.58 ± 0.16	73.77 ± 0.28	73.21 ± 0.32	83.47 ± 0.41	49.12 ± 0.31	0.59 ± 0.04	0.04 ± 0.003
$Z'(350)$	63.83 ± 0.14	55.75 ± 0.16	76.24 ± 0.27	75.05 ± 0.31	95.76 ± 0.43	98.57 ± 0.45	94.40 ± 0.44	18.14 ± 0.06
$Z'(1000)$	67.70 ± 0.15	59.69 ± 0.17	77.32 ± 0.26	77.48 ± 0.30	97.53 ± 0.40	99.95 ± 0.41	99.82 ± 0.41	23.56 ± 0.08
$Z'(1500)$	69.44 ± 0.22	61.38 ± 0.24	78.07 ± 0.36	78.36 ± 0.41	97.93 ± 0.54	99.96 ± 0.55	99.89 ± 0.56	25.50 ± 0.11
$Z'(2000)$	70.79 ± 0.22	62.61 ± 0.24	78.23 ± 0.35	78.70 ± 0.40	98.02 ± 0.53	99.98 ± 0.55	99.92 ± 0.55	26.72 ± 0.12
Efficiencies for $W \rightarrow \mu \nu_\mu$.								
Process	$\epsilon_1 (\times 100)$	$\epsilon_2 (\times 100)$	$\epsilon_3 (\times 100)$	$\epsilon_4 (\times 100)$	$\epsilon_5 (\times 100)$	$\epsilon_6 (\times 100)$	$\epsilon_7 (\times 100)$	$\epsilon_c (\times 100)$
$t\bar{t}h$	64.33 ± 0.14	54.17 ± 0.16	73.85 ± 0.27	73.48 ± 0.31	86.55 ± 0.41	52.17 ± 0.31	0	0
$t\bar{t}/h$	62.19 ± 0.14	53.55 ± 0.16	73.51 ± 0.28	72.93 ± 0.32	83.63 ± 0.41	49.15 ± 0.31	0.60 ± 0.04	0.04 ± 0.002
$Z'(350)$	63.72 ± 0.14	55.68 ± 0.16	76.12 ± 0.27	75.35 ± 0.31	95.81 ± 0.43	98.59 ± 0.45	94.36 ± 0.44	18.13 ± 0.06
$Z'(1000)$	67.79 ± 0.15	59.57 ± 0.17	77.15 ± 0.26	77.70 ± 0.30	97.59 ± 0.40	99.95 ± 0.41	99.84 ± 0.41	23.58 ± 0.08
$Z'(1500)$	69.60 ± 0.21	61.39 ± 0.24	78.04 ± 0.36	78.39 ± 0.41	98.00 ± 0.54	99.98 ± 0.56	99.88 ± 0.56	25.56 ± 0.11
$Z'(2000)$	70.66 ± 0.22	62.58 ± 0.24	78.07 ± 0.35	78.99 ± 0.40	97.99 ± 0.53	99.99 ± 0.55	99.90 ± 0.55	26.70 ± 0.12

The main purpose of applying these selection cuts, as mentioned before, is to be capable to distinguish the signal from other SM processes with the same final states, so it is needed that the efficiency of a certain cut is higher for signals and small for backgrounds in order to reduce the data associated with SM processes, and highlight the signals studied. As seen in Table 9, the first five cuts applied have almost the same efficiencies for signals and backgrounds, which is expected, as the topology of the objects we are analyzing are very similar, because we are tagging tops and leptons, characteristic of $t\bar{t}$ processes. Then, it makes sense the efficiencies for all processes turn out to be similar. In addition, in Figures 30 and 31, plots related the number of events that passed each cut is presented, where

in order to pass a certain cut the event must have passed the immediately previous cut. Here the y – axis is re-scaled to the unit because of the difference on number of events for signals and backgrounds.

Each bin of the distribution presented in Figures 30 and 31 is a subset of the previous one and, as it can be seen from the plots, before applying any cuts, the backgrounds presented greater number of events than the signals. In contrast, after the first 5 cuts (presented in Table 4), the signals barely exceed the numbers of events corresponding to the backgrounds. After the last two cuts on p_T and mass, the backgrounds are completely suppressed and none of the events of the signals get lost in the process. These results show great concordance with the results obtained calculating the efficiencies of the cuts applied (Table 9).

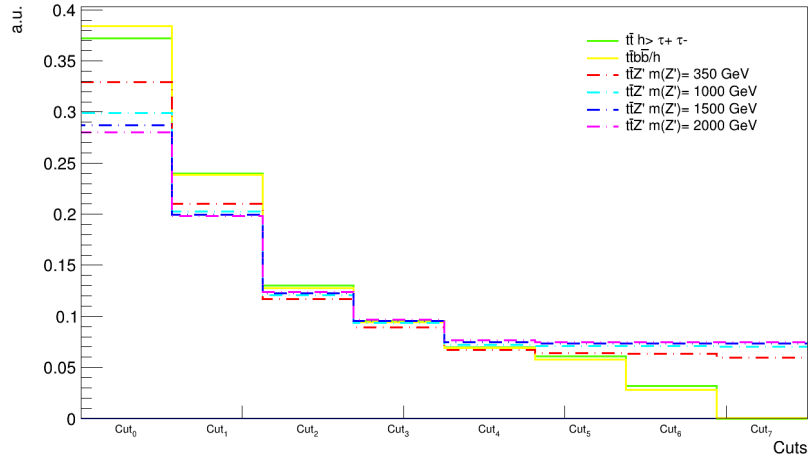


Figure 30: Number of events normalized to the unity that passed each cut (Cuts presented from Table 4 to 8) for $W^\pm \rightarrow e^\pm \nu_e(\bar{\nu}_e)$.

The results for the number of events ($Events$), calculated as in Equation 6.3, after each cut for the signals and the backgrounds are presented in Table 10.

From Table 10 it can be seen that with all seven cuts the backgrounds present lower number of events than two of the signals (for 350 GeV and 1000 GeV $m_{Z'}$) and similar number of events for the other two (for 1500 GeV and 2000 GeV $m_{Z'}$) despite the fact that initially the backgrounds showed much more number of events than the signals. This behavior in the number of events ($Events$) for the backgrounds and signals after the last two cuts is as one would expect, since in the case of the two backgrounds the two taus are produced by the SM mediators, which have a much lower mass than the Z' signals considered. Therefore, the two taus are predicted to have a higher scalar p_T sum and

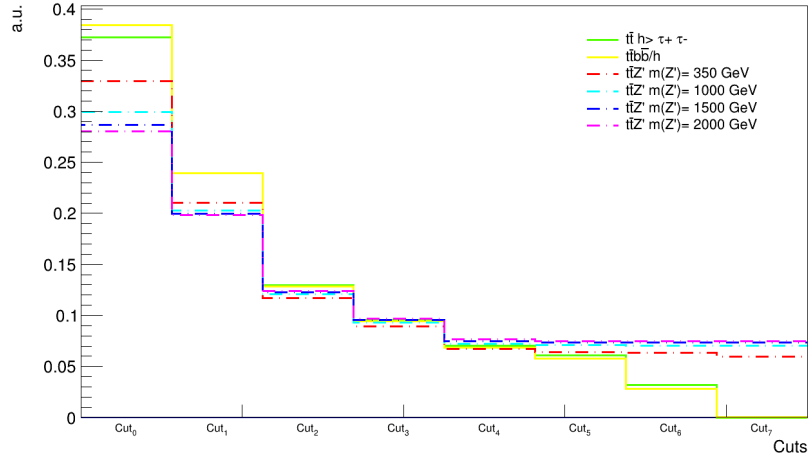


Figure 31: Number of events normalized to the unity that passed each cut (Cuts presented from Table 4 to 8) for $W^\pm \rightarrow \mu^\pm \nu_\mu(\bar{\nu}_\mu)$.

Table 10: Number of events normalized to cross section and luminosity (*Events*) of high mass signals and backgrounds for every cut applied in channels $W^\pm \rightarrow e, \nu_e$ and $W^\pm \rightarrow \mu, \nu_\mu$.

Number of events (<i>Events</i>) for $W^\pm \rightarrow e, \nu_e$.								
Process	No Cuts	Cut ₁	Cut ₂	Cut ₃	Cut ₄	Cut ₅	Cut ₆	Cut ₇
$t\bar{t}h$	654.34	421.54	228.20	168.02	122.93	106.73	55.72	0
$t\bar{t}/h$	785.86	488.11	261.54	192.93	141.25	117.91	57.92	0.34
$Z'(350)$	16.2	10.34	5.76	4.39	3.30	3.16	3.11	2.94
$Z'(1000)$	2.01	1.36	0.81	0.63	0.49	0.47	0.47	0.47
$Z'(1500)$	0.61	0.42	0.26	0.20	0.16	0.15	0.15	0.15
$Z'(2000)$	0.14	0.09	0.06	0.05	0.04	0.04	0.04	0.04
Number of events (<i>Events</i>) for $W^\pm \rightarrow \mu, \nu_\mu$.								
$t\bar{t}h$	654.34	420.92	228.04	168.41	123.75	107.11	55.88	0
$t\bar{t}/h$	785.86	488.72	261.73	192.41	140.33	117.36	57.69	0.34
$Z'(350)$	16.2	10.32	5.75	4.37	3.30	3.16	3.11	2.94
$Z'(1000)$	2.01	1.36	0.81	0.63	0.49	0.47	0.47	0.47
$Z'(1500)$	0.61	0.42	0.26	0.20	0.16	0.15	0.15	0.15
$Z'(2000)$	0.14	0.10	0.06	0.05	0.04	0.04	0.04	0.04

higher reconstructed mass as can be seen from Figure 6.1, such that these cuts leave higher mass signals unaltered. These results are equivalent to the efficiency results, as the Relative efficiency on each cut for backgrounds tended each time closer to zero, while the efficiency for signals increased towards 1 (or 100 in percentages).

Now for the low mass signals the efficiency and cumulative efficiency for all cuts were also calculated. In this case, the total number of cuts is five, and the results are

presented in Table 11. The results obtained show that the efficiency of the cuts applied for signals and background is roughly the same, due to the fact that these cuts were not designed specifically for background suppression, but rather to distinguish $t\bar{t}$ processes and to fulfill the requirements of the CMS and ATLAS detectors. From Table 11, just as for high mass signals, it can be seen that the efficiencies of all the applied selection criteria, and subsequently the cumulative efficiency as well, are almost identical for the two channels. Since there is only one pair of final state taus, there is no added complexity when tagging the particles coming from the different W decays, which could lead to a wrong W reconstruction, resulting in smaller efficiencies for either of the channels. Also, considering the fact that both m_e and m_μ are much more smaller than m_W , they both exhibit similar kinematic distributions (p_T , E, etc), then it is assumed that they both present similar efficiencies when applying the same cuts to both of them. On the other hand, none of the cuts present a significant difference in its efficiency between signals and backgrounds as explained earlier due to the nature of the cuts.

Table 11: Relative efficiencies in percentages for the two considered backgrounds and the signals of low mass processes and the cumulative efficiency ϵ_c .

Efficiencies for $W \rightarrow e \nu_e$.						
Process	$\epsilon_1 (\times 100)$	$\epsilon_2 (\times 100)$	$\epsilon_3 (\times 100)$	$\epsilon_4 (\times 100)$	$\epsilon_5 (\times 100)$	$\epsilon_c (\times 100)$
$t\bar{t}h$	64.32 ± 0.06	54.20 ± 0.07	73.70 ± 0.12	73.20 ± 0.14	86.69 ± 0.18	16.30 ± 0.03
$t\bar{t}/h$	62.16 ± 0.06	53.65 ± 0.07	73.67 ± 0.12	73.17 ± 0.14	83.54 ± 0.18	15.02 ± 0.03
$Z'(150)$	62.35 ± 0.20	54.04 ± 0.23	75.07 ± 0.39	74.06 ± 0.45	89.27 ± 0.60	16.72 ± 0.09
$Z'(200)$	62.62 ± 0.20	54.34 ± 0.23	75.21 ± 0.39	74.38 ± 0.45	92.67 ± 0.61	17.64 ± 0.09
$Z'(250)$	62.85 ± 0.20	54.76 ± 0.23	75.58 ± 0.39	74.50 ± 0.45	94.24 ± 0.61	18.26 ± 0.09
$Z'(300)$	63.42 ± 0.20	55.42 ± 0.23	75.66 ± 0.39	74.73 ± 0.44	95.17 ± 0.61	18.91 ± 0.09
Efficiencies for $W \rightarrow \mu \nu_\mu$.						
Process	$\epsilon_1 (\times 100)$	$\epsilon_2 (\times 100)$	$\epsilon_3 (\times 100)$	$\epsilon_4 (\times 100)$	$\epsilon_5 (\times 100)$	$\epsilon_c (\times 100)$
$t\bar{t}h$	64.39 ± 0.06	54.20 ± 0.07	73.77 ± 0.12	73.24 ± 0.14	86.72 ± 0.18	16.35 ± 0.03
$t\bar{t}/h$	62.16 ± 0.06	53.51 ± 0.07	73.68 ± 0.12	73.15 ± 0.14	83.64 ± 0.18	14.99 ± 0.02
$Z'(150)$	62.38 ± 0.20	54.37 ± 0.23	74.99 ± 0.39	73.99 ± 0.45	89.51 ± 0.60	16.84 ± 0.09
$Z'(200)$	62.63 ± 0.20	54.61 ± 0.23	75.61 ± 0.39	74.15 ± 0.45	92.77 ± 0.61	17.79 ± 0.09
$Z'(350)$	62.82 ± 0.20	54.70 ± 0.23	75.69 ± 0.39	74.69 ± 0.45	94.14 ± 0.61	18.29 ± 0.09
$Z'(2000)$	63.33 ± 0.20	55.29 ± 0.23	75.68 ± 0.39	74.51 ± 0.44	95.25 ± 0.61	18.81 ± 0.094

A plot of the efficiencies of the cuts used for the low mass limit are shown in Figures 32 and 31, where the behaviors agree with the results obtained in Table 11 and the number of events that passed each cut (which is normalized to one) is almost the same for every cut.

In Table 12 is shown the number of events resulting after applying each cut. It can be seen that, since the cuts applied to the low mass signals are not designed specifically for $t\bar{t}$ background suppression, the number of events for the backgrounds, obtained after all the

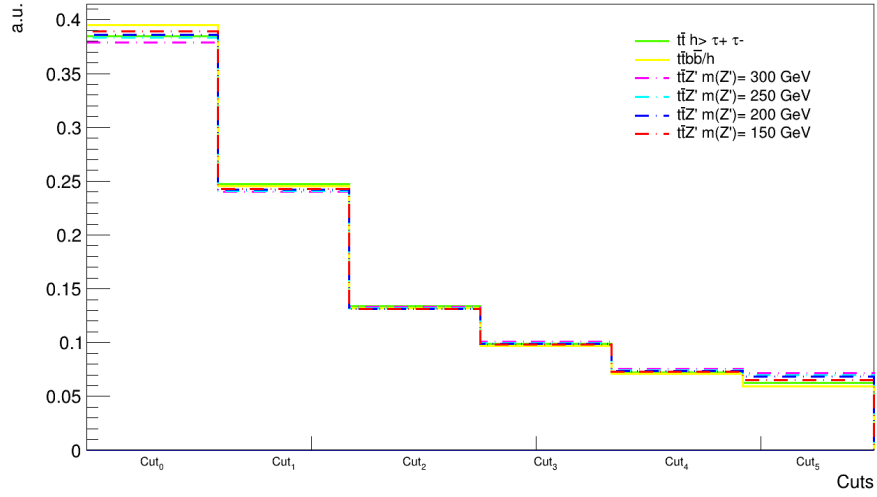


Figure 32: Number of events normalized to the unity that passed each cut (Cuts presented from Table 4 to 8) for $W^\pm \rightarrow e^\pm \nu_e(\bar{\nu}_e)$ for the low mass signals (i.e. $m_{Z'} \leq 300 \text{ GeV}$).

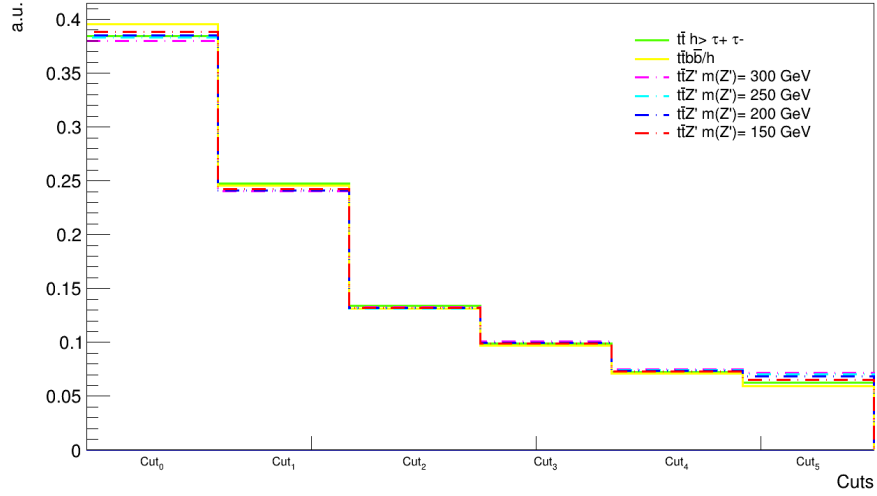


Figure 33: Number of events normalized to the unity that passed each cut (Cuts presented from Table 4 to 8) for $W^\pm \rightarrow \mu^\pm \nu_\mu(\bar{\nu}_\mu)$ for the low mass signals (i.e. $m_{Z'} \leq 300 \text{ GeV}$).

cuts, is similar to the initial number of events, and there is no significant improvement in the signal number of events. Consequently, these cuts are not relevant for signal distinguishability.

Table 12: Table containing the number of events defined as in Equation 6.3 for each cut applied to all the backgrounds and signals of low mass category.

Number of events (<i>Events</i>) for $W^\pm \rightarrow e, \nu_e$.						
Process	No Cuts	Cut ₁	Cut ₂	Cut ₃	Cut ₄	Cut ₅
$t\bar{t}h$	654.34	420.85	228.10	168.11	123.06	106.70
$t\bar{t}/h$	785.86	488.53	262.10	193.09	141.28	118.03
$Z'(150)$	49.98	31.16	16.84	12.64	9.36	8.36
$Z'(200)$	42.34	26.52	14.41	10.84	8.06	7.47
$Z'(250)$	25.04	15.74	8.62	6.51	4.85	4.57
$Z'(300)$	19.99	12.68	7.03	5.32	3.97	3.78
Number of events (<i>Events</i>) for $W^\pm \rightarrow \mu, \nu_\mu$.						
$t\bar{t}h$	654.34	421.34	228.40	168.48	123.40	107.01
$t\bar{t}/h$	785.86	488.53	261.40	192.61	140.89	117.85
$Z'(150)$	49.98	31.18	16.95	12.71	9.41	8.42
$Z'(200)$	42.34	26.52	14.48	10.95	8.12	7.53
$Z'(250)$	25.04	15.73	8.61	6.51	4.86	4.58
$Z'(300)$	19.99	12.66	7.00	5.30	3.95	3.76

6.5 Significances

The figure of merit used for this analysis is the significance S^{ch} defined as:

$$S^{ch} = \frac{N_{sig}}{\sqrt{N_{sig}^2 + N_{bkg}^2 + (0.25N_{bkg})^2}}, \quad (6.6)$$

for each signal, where ch represents the channel we are looking at (i.e. $W^\pm \rightarrow e, \nu_e$ or $W^\pm \rightarrow \mu, \nu_\mu$), N_{sig} is the number of events of the signal and N_{bkg} is the total number of events of the backgrounds considered, such that $N_{bkg} = N_{bkg_1} + N_{bkg_2}$. Making use of the plots showed in Figures 28a, 28b for high mass and Figures 29a and 29b for low mass signals, data obtained for the significance calculated for each bin of mass reconstruction was plotted as shown in Figures 34 and 35.

This analysis of the significance allows us to determine how prevalent is the signal over the noise, hence the main goal is to obtain high significance values. From the plots generated for the significance per bin it is notable that the highest significance values are presented around the values of mass of each signal and that the significance presented well defined peaks. To make an approximate analysis of the expected significance of the signals, we took a combined significance of the peak bins defined as:

$$\sigma_{tot}^{ch_j} = \frac{\sum_{i=1}^{n_j} S_i^{ch_j}}{\sqrt{n_j}} \quad (6.7)$$

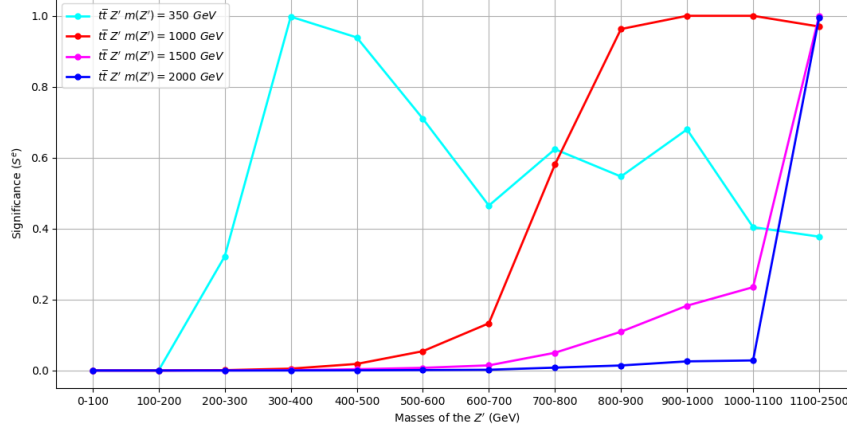
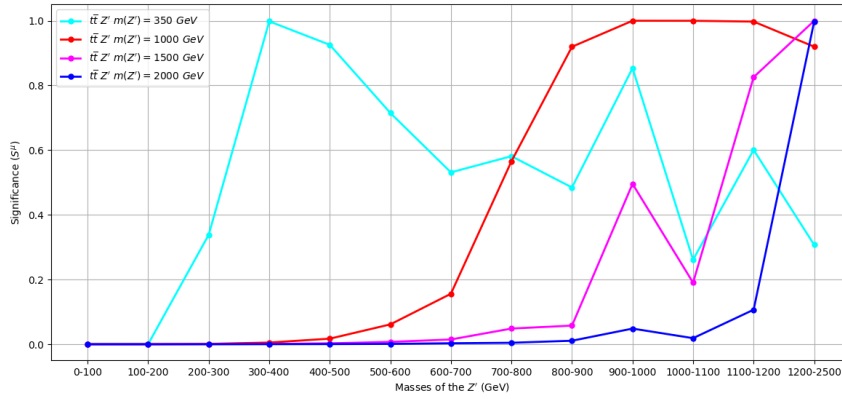
(a) Significance per bin of the reconstructed mass plots for the $W^\pm \rightarrow e, \nu_e$ channel.(b) Significance per bin of the reconstructed mass plots for the $W^\pm \rightarrow \mu, \nu_\mu$ channel.

Figure 34: Figures (a) and (b) show the values of significance S^e and S^μ respectively, calculated for each bin of the mass plot, for the four different $m_{Z'}$ considered in the high mass classification.

in order to obtain a cumulative significance for a single signal and its j -th channel where i corresponds to the i -th bin and n_j is the number of bins taken for that channel. The significances obtained for both high mass signals and low mass signals is presented in Table 13.

Table 13: Total significances (σ_{tot}) of both channels: $W^\pm \rightarrow e, \nu_e$ denoted with the superscript e and $W^\pm \rightarrow \mu, \nu_\mu$ denoted with the superscript μ , for all the signals studied.

High mass signals			Low mass signals		
Process	σ_{tot}^e	σ_{tot}^μ	Process	σ_{tot}^e	σ_{tot}^μ
$Z'(350)$	1.53	1.52	$Z'(150)$	0.69	0.95
$Z'(1000)$	1.97	2.16	$Z'(200)$	1.38	1.28
$Z'(1500)$	1.00	1.29	$Z'(250)$	1.38	1.41
$Z'(2000)$	0.99	1.00	$Z'(300)$	1.64	1.63

Equation 6.7 is an statistical approximation to a profile binned likelihood, it has as a

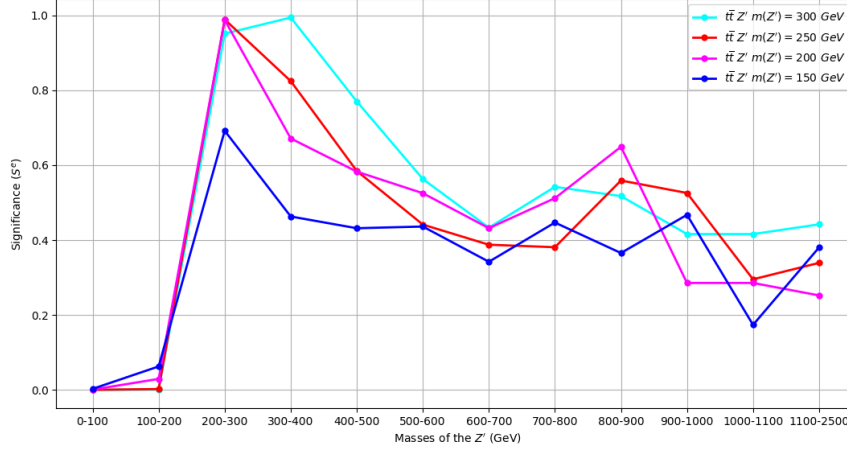
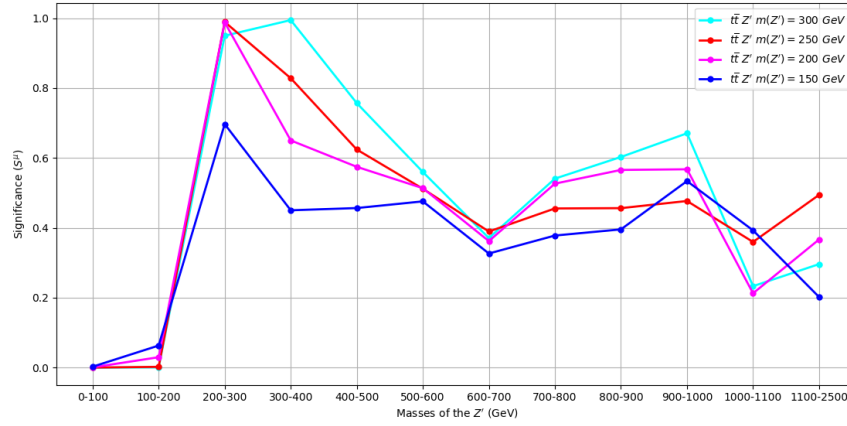
(a) Significance as a function of $m_{Z'}$ on the $W^{\pm} \rightarrow e, \nu_e$ channel.(b) Significance as a function of $m_{Z'}$ on the $W^{\pm} \rightarrow \mu, \nu_{\mu}$ channel.

Figure 35: Figures (a) and (b) show the value of the Significance (S^e and S^{μ} respectively) per bin on the reconstructed mass plots for all low mass signals.

denominator $\sqrt{n_j}$ to make the combination of bins as the total sum of the significance values over the ratio of bins taking $\sqrt{n_j}$ as an approximation of a poissonian error in measurement. Once again, this calculation allows us to estimate how relevant our signals are over the backgrounds, we can generalize this combined significance definition to multiple channels as:

$$\sigma_{tot}^{\sum ch_j} = \frac{\sum_{j=1}^m \sum_{i=1}^{n_j} S_i^{ch_j}}{\sqrt{\sum_{j=1}^m n_j}} \quad (6.8)$$

where m is the total number of channels we are considering. The resulting combined significances for the two channels considered in this thesis ($W \rightarrow e \nu_e$ and $W \rightarrow \mu \nu_{\mu}$) are shown in Table 14a and this combined significances ($\sigma_{tot}^{e+\mu}$) are plotted as a function of the Z' mass in Figure 36, where it can be observed that the highest significance values were

found for a Z' with a mass of $m_{Z'} = 1000$ GeV.

The behavior of the plots on Figure 36 show a general increment of the significance proportional to the mass value of the signal, nonetheless when approaching mass values greater than 1000 GeV the significance value decreases and tends to one for the masses that present peaks that fall on the overflow bin. These plots also present a $\sigma_{tot}^{e_\tau + \mu_\tau + e_\mu + \mu_\mu}$ significance which corresponds to the combined significance of the signals showed in Figure 8 and two extra processes which correspond to the top annihilation resulting in a pair of muons, i.e. signals such that $Z' \rightarrow \mu^+ \mu^-$. Here we denote e_τ and μ_τ as the $W \rightarrow e \nu_e$ and $W \rightarrow \mu \nu_\mu$ channels of the process $Z' \rightarrow \tau^+ \tau^-$ and $e_\mu \mu_\mu$ for $W \rightarrow e \nu_e$ and $W \rightarrow \mu \nu_\mu$ channels respectively for the process $Z' \rightarrow \mu^+ \mu^-$. The combined significances for each signal of the four channels is presented in Table 14b.

(a) Combined significance, for the two W decays combined (e + μ) studied for each signal generated in the Z' tau decay.

High mass signals		Low mass signals	
Process	$\sigma_{tot}^{e+\mu}$	Process	$\sigma_{tot}^{e+\mu}$
$Z'(350)$	2.16	$Z'(150)$	1.18
$Z'(1000)$	2.92	$Z'(200)$	1.88
$Z'(1500)$	1.63	$Z'(250)$	1.98
$Z'(2000)$	1.41	$Z'(300)$	2.31

(b) Combined significance, for two Z' decays ($Z' \rightarrow \tau^+ \tau^-$ and $Z' \rightarrow \mu^+ \mu^-$) and the two considered W decays.

High mass signals		Low mass signals	
Process	$\sigma_{tot}^{e_\tau + \mu_\tau + e_\mu + \mu_\mu}$	Process	$\sigma_{tot}^{e_\tau + \mu_\tau + e_\mu + \mu_\mu}$
$Z'(350)$	2.34	$Z'(150)$	-
$Z'(1000)$	3.03	$Z'(200)$	-
$Z'(1500)$	1.92	$Z'(250)$	-
$Z'(2000)$	-	$Z'(300)$	-

Table 14: Tables of all the different combined significances $\sigma_{tot}^{ch_j}$ calculated as in Equation 6.8, for both high and low mass categories.

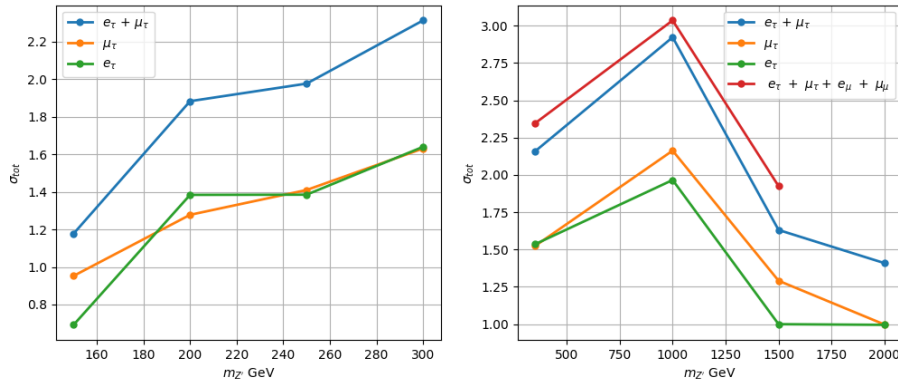


Figure 36: Plots of the combined significance for all the different group of channels. $W \rightarrow e \nu_e$ alone, $W \rightarrow \mu \nu_\mu$ alone, $W \rightarrow e \nu_e + W \rightarrow \mu \nu_\mu$ together and $W \rightarrow e \nu_e + W \rightarrow \mu \nu_\mu$ for both $Z' \rightarrow \tau^+ \tau^-$ and $Z' \rightarrow \mu^+ \mu^-$ processes. The names of the legend represent each superscript on the σ_{tot} notation.

7 Conclusions

A Covariant notation

As quantum fields are defined over space and time, we shall work in what is known as **covariant notation**, in which x^μ ($\mu = 0, 1, 2, 3$) corresponds to a four-vector where $x^0 = ct$ denotes the time component and the space components are x^j ($j = 1, 2, 3$), i.e. $x^\mu = (ct, \mathbf{x})$. The components of four-vectors will be labelled by Greek indices, the components of spatial three-vectors by Latin indices.

In general, the four-vector inner product is,

$$x \cdot y = x^0 y^0 - \mathbf{x} \cdot \mathbf{y},$$

which can also be expressed as

$$x \cdot y = g_{\mu\nu} x^\mu y^\nu,$$

where $g_{\mu\nu}$ is the metric tensor, with components

$$\left. \begin{aligned} g_{00} &= -g_{11} = -g_{22} = -g_{33} = +1 \\ g_{\mu\nu} &= 0 \text{ if } \mu \neq \nu \end{aligned} \right\}$$

Covariant x_μ and contravariant x^μ vectors are related via the metric tensor as:

$$x_\mu = \sum_{\nu=0}^3 g_{\mu\nu} x^\nu \equiv g_{\mu\nu} x^\nu$$

Where in the last part of the equation Einstein's summation convention is used: repeated Greek indices, one contravariant and one covariant are always summed over. For the metric tensor we also have:

$$g^{\lambda\mu} g_{\mu\nu} = g_\nu^\lambda = \delta_\nu^\lambda$$

where δ_ν^λ is the usual Kronecker delta: $\delta_\nu^\lambda = 1$ if $\lambda = \nu$, and $\delta_\nu^\lambda = 0$ if $\lambda \neq \nu$. From the metric tensor definition we can write

$$x^0 = x_0 \quad x^i = -x_i,$$

and hence

$$x \cdot y = g_{\mu\nu} x^\mu y^\nu = x_\mu y^\mu = x^\mu y_\mu.$$

Also $x \cdot y = g^{\mu\nu} x_\mu y_\nu$ and $g_{\mu\nu} = g^{\mu\nu}$. As we aim to work with covariant theories, we require that quantities should be Lorentz covariant if they are to transform appropriately

under the elements of the Lorentz group [2]. Under a Lorentz transformation we have the following transformations:

1. *Scalars*: A scalar is a number, and it will have the same value regardless of the inertial frame. It is thus said to be Lorentz invariant (for example: the electric charge and rest mass of a particle).
2. *Four-vectors*: The Lorentz transformation of a four-vector can be written in matrix form as

$$\begin{pmatrix} x'^0 \\ x'^1 \\ x'^2 \\ x'^3 \end{pmatrix} = \begin{pmatrix} \gamma & -\beta\gamma & 0 & 0 \\ -\beta\gamma & \gamma & 0 & 0 \\ 0 & 0 & 1 & 0 \\ 0 & 0 & 0 & 1 \end{pmatrix} \begin{pmatrix} x^0 \\ x^1 \\ x^2 \\ x^3 \end{pmatrix}$$

or also in a more compact way as

$$x'^\mu = \Lambda^\mu_\nu x^\nu,$$

where $\Lambda^\mu_\nu \equiv (\partial x'^\mu / \partial x^\nu)$. The Lorentz transformation leaves the length of the four-vector x invariant, i.e.

$$|x|^2 = x^\mu x_\mu = (x^0)^2 - (x^1)^2 - (x^2)^2 - (x^3)^2 = |x'|^2.$$

An important example would be the four-dimensional generalization of the gradient operator ∇ ,

$$\frac{\partial \phi}{\partial x^\mu} \equiv \partial_\mu \phi,$$

which is a covariant four-vector for ϕ being, for example, a scalar function. And it also transforms like a four-vector.

$$\frac{\partial \phi}{\partial x'^\mu} = \left(\frac{\partial x^\nu}{\partial x'^\mu} \right) \frac{\partial \phi}{\partial x^\nu} \quad [13].$$

B Euler-Lagrange equations for fields

The equations of motion for the field theory can be derived just as the classical equations are, through the principle of least action, i.e. keeping the Action \mathcal{A} stationary against small variations of the fields, let's consider the following variations

$$\phi^A(x) \rightarrow \phi^A(x) + \delta\phi^A(x) \quad (\text{B.1})$$

$$\partial_\mu \phi^A(x) \rightarrow \partial_\mu \phi^A(x) + \partial_\mu \delta\phi^A(x), \quad (\text{B.2})$$

with these variations in order to keep \mathcal{A} invariant it is expected that $\delta\phi^A$ vanishes on the boundary of $\delta\Omega$. From Equation (2.9) we can write variations of the Action \mathcal{A} as:

$$\delta\mathcal{A} = \int_{\Omega} d^4x \left[\frac{\partial\mathcal{L}}{\partial\phi^A} \delta\phi^A + \frac{\partial\mathcal{L}}{\partial(\partial_\mu\phi^A)} \partial_\mu \delta\phi^A \right], \quad (\text{B.3})$$

which can be rewritten as,

$$= \int_{\Omega} d^4x \frac{\partial\mathcal{L}}{\partial\phi^A} \delta\phi^A - \partial_\mu \left(\frac{\partial\mathcal{L}}{\partial(\partial_\mu\phi^A)} \right) \delta\phi^A + \partial_\mu \left(\frac{\partial\mathcal{L}}{\partial(\partial_\mu\phi^A)} \delta\phi^A \right), \quad (\text{B.4})$$

$$(\text{B.5})$$

$$= \int_{\Omega} d^4x \left[\frac{\partial\mathcal{L}}{\partial\phi^A} - \partial_\mu \left(\frac{\partial\mathcal{L}}{\partial(\partial_\mu\phi^A)} \right) \right] \delta\phi^A + \int_{\Omega} d^4x \partial_\mu \left[\frac{\partial\mathcal{L}}{\partial(\partial_\mu\phi^A)} \delta\phi^A \right] \quad (\text{B.6})$$

where the last term of the last equality vanishes due to Gauss theorem, as the integral becomes an integral over $\delta\Omega$ and $\delta\phi^A$ vanishes on $\delta\Omega$. So we are left with:

$$\delta\mathcal{A} = \int_{\Omega} d^4x \left[\frac{\partial\mathcal{L}}{\partial\phi^A} - \partial_\mu \left(\frac{\partial\mathcal{L}}{\partial(\partial_\mu\phi^A)} \right) \right] \delta\phi^A = 0 \quad (\text{B.7})$$

As taking $\delta\phi^A = 0$ would be rather trivial the term multipliynng it is the one that needs to vanish and so it is obtained that:

$$\partial_\mu \left(\frac{\partial\mathcal{L}}{\partial(\partial_\mu\phi^A)} \right) = \frac{\partial\mathcal{L}}{\partial\phi^A}. \quad (\text{B.8})$$

which are the Euler-lagrange equations presented in Chapter 2.2.2.

C Hamiltonian formalism; Legendre transformation

The Legendre transformation is used to convert functions of one quantity into functions of the conjugate quantity, for example: position, pressure, or temperature into momentum, volume, and entropy. Lets consider a function of two independent variables $f(x, y)$ so that

the total differential of the function is

$$df = \left(\frac{\partial f}{\partial x} \right)_y dx + \left(\frac{\partial f}{\partial y} \right)_x dy, \quad (\text{C.1})$$

where defining $u = \frac{\partial f}{\partial x}$, $v = \frac{\partial f}{\partial y}$, Equation C.1 can be written as

$$df = udx + vdy \quad (\text{C.2})$$

where u (v) is the conjugate of x (y), so we wish to change the basis of description from (x, y) to (u, y) for this we compute the differential:

$$d(ux) = xdu + udx, \quad (\text{C.3})$$

and subtract this equation from Equation C.2, such that

$$df - d(ux) = d(f - ux) = dg = vdy - xdu, \quad (\text{C.4})$$

where the function $g = f - ux$ is the Legendre-transformed function that depends on (u, y) as we wanted. The equation C.4 has the exactly form desired and now the quantities x and v can be defined in terms of u and y , giving the relations:

$$x = -\frac{\partial g}{\partial u}, \quad v = \frac{\partial g}{\partial y}. \quad (\text{C.5})$$

This exact same procedure is done to go from (q_r, \dot{q}_r, t) to (q_r, p_r, t) and obtain the Hamiltonian, i.e. the Legendre-transformed function of the Lagrangian.

D Noether's theorem demonstration

When performing an infinitesimal transformation of the coordinate system under which the fields transform as

$$\Phi^A \rightarrow \Phi'^A = \Phi^A + \delta\Phi^A. \quad (\text{D.1})$$

where $\delta\Phi^A$ is an infinitesimal variation. This transformation is considered a symmetry if it leaves equations of motion invariant i.e. if the Lagrangian changes by a total derivative,

$$\mathcal{L} \rightarrow \mathcal{L}' = \mathcal{L} + \partial_\mu \mathcal{J}^\mu; \quad \delta\mathcal{L} = \partial_\mu \mathcal{J}^\mu, \quad (\text{D.2})$$

for a set function $\mathcal{J}^\mu(\phi^A)$, with this transformations a variation in the Lagrangian,

just as the Lagrangian itself, depends on both ϕ and $\partial_\mu\phi$ and can be written as:

$$\delta\mathcal{L} = \frac{\partial\mathcal{L}}{\partial\phi^A}\delta\phi^A + \frac{\partial\mathcal{L}}{\partial(\partial_\mu\phi^A)}\partial_\mu(\delta\phi^A) \quad (\text{D.3})$$

$$(\text{D.4})$$

$$= \left[\frac{\partial\mathcal{L}}{\partial\phi^A} - \partial_\mu \frac{\partial\mathcal{L}}{\partial(\partial_\mu\phi^A)} \right] \delta\phi^A + \partial_\mu \left(\frac{\partial\mathcal{L}}{\partial(\partial_\mu\phi^A)} \delta\phi^A \right). \quad (\text{D.5})$$

From the Euler-Lagrange equations

$$\partial_\mu \left(\frac{\partial\mathcal{L}}{\partial(\partial_\mu\phi^A)} \right) = \frac{\partial\mathcal{L}}{\partial\phi^A}, \quad (\text{D.6})$$

the first term in Equation D.5 vanishes and the Lagrangian variation becomes:

$$\delta\mathcal{L} = \partial_\mu \left(\frac{\partial\mathcal{L}}{\partial(\partial_\mu\phi^A)} \delta\phi^A \right), \quad (\text{D.7})$$

and by definition $\delta\mathcal{L} = \partial_\mu\mathcal{J}^\mu$ and consequently we obtain that:

$$\partial_\mu j^\mu = 0 \quad \text{with} \quad j^\mu = \frac{\partial\mathcal{L}}{\partial(\partial_\mu\phi^A)}\delta\phi^A - \mathcal{J}^\mu(\phi), \quad (\text{D.8})$$

j^μ is known as Noether's current and it corresponds to a conserved quantity [13]. This conservation law can also be expressed in terms of a conserved charge or a Noether's charge which is constant in time:

$$Q \equiv \int_{\Omega} j^0 d^3x. \quad (\text{D.9})$$

If one considers an infinitesimal translation DE PORNTONER TONG.

References

- [1] Y. Nagashima and Y. Nambu. *Elementary Particle Physics: Quantum Field Theory and Particles V1*. Number v. 1. Wiley, 2010.
- [2] T. Lancaster, S.J. Blundell, and S. Blundell. *Quantum Field Theory for the Gifted Amateur*. OUP Oxford, 2014.
- [3] Satyendra Nath Bose. *Plancks Gesetz und Lichtquantenhypothese*, volume 26. Zeitschrift für Physik, 1924.
- [4] Paul Adrien Maurice Dirac and Ralph Howard Fowler. *On the theory of quantum mechanics*, volume 112. Proceedings of the Royal Society of London. Series A, Containing Papers of a Mathematical and Physical Character, 1926.
- [5] C. Cohen-Tannoudji, B. Diu, B. Dui, F. Laloë, S.R. Hemley, N. Ostrowsky, and D.B. Ostrowsky. *Quantum Mechanics*. Number v. 2 in A Wiley interscience publication. Wiley, 1977.
- [6] P. Langacker. *The Standard Model and Beyond*. Series in High Energy Physics, Cosmology and Gravitation. CRC Press, 2009.
- [7] R.N. Mohapatra. *Unification and Supersymmetry: The Frontiers of Quark-Lepton Physics*. Graduate Texts in Contemporary Physics. Springer New York, 2006.
- [8] A. Lahiri and P.B. Pal. *A First Book of Quantum Field Theory*. Alpha Science International, 2005.
- [9] H. Goldstein. *Classical Mechanics*. Pearson Education, 2002.
- [10] J.W Belcher S. Liao, P. Dourmashkin. *Electricity and magnetism: Fields*. MIT Online, 2004.
- [11] D. Goldberg. *The Standard Model in a Nutshell*. In a Nutshell. Princeton University Press, 2017.
- [12] M. Thomson. *Modern Particle Physics*. Modern Particle Physics. Cambridge University Press, 2013.
- [13] F. Mandl and G. Shaw. *Quantum Field Theory*. A Wiley-Interscience publication. Wiley, 2010.

-
- [14] Tomáš Brauner. *Spontaneous Symmetry Breaking and Nambu–Goldstone Bosons in Quantum Many-Body Systems*, volume 2. Symmetry, Apr 2010.
- [15] R Alkofer and J Greensite. *Quark confinement: the hard problem of hadron physics*, volume 34. Journal of Physics G: Nuclear and Particle Physics, May 2007.
- [16] D. Griffiths. *Introduction to Elementary Particles*. John Wiley Sons Inc., 1987.
- [17] Ennio Salvioni, Giovanni Villadoro, and Fabio Zwirner. *Minimal Z models: present bounds and early LHC reach*, volume 2009. Journal of High Energy Physics, Nov 2009.
- [18] Zack Sullivan. *Fully differential W' production and decay at next-to-leading order in QCD*, volume 66. Phys. Rev. D, Oct 2002.
- [19] Ya-Bing Zuo, Chong-Xing Yue, Wei Yang, Yan-Nan Hao, and Wei-Rong Zhang. *New gauge boson W' and radiative leptonic decays of charged B and D mesons*, volume 78. Eur. Phys. J. C, 2018.
- [20] Daniel Hayden, Raymond Brock, and Christopher Willis. *Z Prime: A Story*. 2013.
- [21] Kenneth Lane. *An introduction to technicolor*. The Building Blocks of Creation, Oct 1994.
- [22] Daniel Duffy and Zack Sullivan. *Model independent reach for W bosons at the LHC*, volume 86. Physical Review D, Oct 2012.
- [23] Kenneth Lane. *Two Lectures on Technicolor*. 2 2002.
- [24] Nick Evans. *Strong extended technicolour interactions and the vertex*, volume 331. Physics Letters B, Jul 1994.
- [25] Lisa Randall and Raman Sundrum. *Large Mass Hierarchy from a Small Extra Dimension*, volume 83. Physical Review Letters, Oct 1999.
- [26] Stephan J. Huber, Chin-Aik Lee, and Qaisar Shafi. *Kaluza-Klein excitations of W and Z at the LHC?*, volume 531. Phys. Lett. B, 2002.
- [27] Andreas Papaefstathiou and Seyi Latunde-Dada. *NLO production of W-prime bosons at hadron colliders using the MC@NLO and POWHEG methods.*, volume 2009. Journal of High Energy Physics, Jul 2009.
- [28] V.M. Abazov, B. Abbott, B.S. Acharya et al. *Search for $W' \rightarrow tb$ resonances with left- and right-handed couplings to fermions*, volume 699. Physics Letters B, 2011.

-
- [29] Maxim Perelstein. *Little Higgs models and their phenomenology*, volume 58. Progress in Particle and Nuclear Physics, Jan 2007.
- [30] Morgan Svensson Seth. *A first study of Hidden Valley models at the LHC*. 2011.
- [31] Hoang Ngoc Long. *The 331 model with right handed neutrinos*, volume 53. Phys. Rev. D, 1996.
- [32] Nady Bakhet, M. Khlopov, and Tarek Hussein. *Search for New Charged Gauge Boson W' via Phenomenology of the Left-Right Symmetric Model at Hadron Colliders*. Jun 2014.
- [33] Paul Langacker. *The physics of heavy Z' gauge bosons*, volume 81. Reviews of Modern Physics, Aug 2009.
- [34] J. Diaz-Cruz, Javier Hernandez-Lopez, and J. Orduz-Ducua. *An extra Z' gauge boson as a source of Higgs particles*, volume 40. Journal of Physics G Nuclear Physics, 03 2013.
- [35] A. Leike. The phenomenology of extra neutral gauge bosons. *Physics Reports*, 317(3-4):143–250, Aug 1999.
- [36] ATLAS Collaboration. *Prospects for searches for heavy Z' and W' bosons in fermionic final states with the ATLAS experiment at the HL-LHC*. Number ATL-PHYS-PUB-2018-044. Geneva, Dec 2018.
- [37] Marcela Carena, Alejandro Daleo, Bogdan A. Dobrescu, and Tim M. P. Tait. *Z' gauge bosons at the Fermilab Tevatron*, volume 70. Physical Review D, Nov 2004.
- [38] Johana Alwall, Michel Herquet, Fabio Maltoni, Olivier Mattelaer, and Tim Stelzer. *MadGraph 5: going beyond*, volume 40. Journal of High Energy Physics, Jun 2011.
- [39] G. Aad, B. Abbott, D. C. Abbott, A. Abed Abud, and et al. *Search for new resonances in mass distributions of jet pairs using 139 fb1 of pp collisions at $s\sqrt{s} = 13$ TeV with the ATLAS detector*, volume 2020. Journal of High Energy Physics, Mar 2020.
- [40] G. Aad, B. Abbott, D. C. Abbott, A. Abed Abud, and et al. *Search for $t\bar{t}$ resonances in fully hadronic final states in pp collisions at $\sqrt{s} = 13$ TeV with the ATLAS detector*, volume 2020. Journal of High Energy Physics, Oct 2020.
- [41] Kenneth Lane and Estia Eichten. *Natural topcolor-assisted technicolor*, volume 352. Physics Letters B, Jun 1995.

-
- [42] Junjie Cao, Zhaohua Xiong, and Jin Min Yang. *Probing top-color-assisted technicolor from top-charm associated production at the CERN Large Hadron Collider*, volume 67. Physical Review D, Apr 2003.
 - [43] Ana López. *LHCb sees new form of matter–antimatter asymmetry in strange beauty particles*. CERN, 2020.
 - [44] Cheng-Wei Chiang, Xiao-Gang He, and German Valencia. *Zmodel forb \rightarrow s $^-$ flavor anomalies*, volume 93. Physical Review D, Apr 2016.
 - [45] P. Ko, Yuji Omura, Yoshihiro Shigekami, and Chaehyun Yu. *LHCb anomaly and B physics in flavored Z models with flavored Higgs doublets*, volume 95. Physical Review D, Jun 2017.
 - [46] Ye Li, Frank Petriello, and Seth Quackenbush. *Reconstructing a Z' Lagrangian using the LHC and low-energy data*, volume 80. Physical Review D, Jun 2009.
 - [47] Johan Alwall, Pavel Demin, Simon de Visscher, Rikkert Frederix, Michel Herquet, Fabio Maltoni, Tilman Plehn, David L Rainwater, and Tim Stelzer. *MadGraph/MadEvent v4: the new web generation*, volume 2007. Journal of High Energy Physics, Sep 2007.
 - [48] Eric Conte, Benjamin Fuks, and Guillaume Serret. *MadAnalysis 5, A User-Friendly Framework for Collider Phenomenology*, volume 184. Comput. Phys. Commun., 2013.
 - [49] I. Antcheva, M. Ballintijn, B. Bellenot, M. Biskup, R. Brun, N. Buncic, Ph. Canal, D. Casadei, O. Couet, V. Fine, and et al. *ROOT — A C++ framework for petabyte data storage, statistical analysis and visualization*, volume 180. Computer Physics Communications, Dec 2009.
 - [50] Giordon Holtsberg Stark. *The search for supersymmetry in hadronic final states using boosted object reconstruction*. May 2018. Presented 26 Apr 2018.
 - [51] L. Rossi. *The LHC superconducting magnets*, volume 030512. Conf. Proc. C, 2003.
 - [52] Naeem Tahir, Joab Sancho, Alexander Shutov, Rüdiger Schmidt, and A. Piriz. *Impact of high energy high intensity proton beams on targets: Case studies for Super Proton Synchrotron and Large Hadron Collider*, volume 15. Physical Review Special Topics - Accelerators and Beams, 05 2012.
 - [53] W. Herr and B. Muratori. *CERN Accelerator School and DESY Zeuthen: Accelerator Physics: Concept of luminosity*. 9 2003.

- [54] Lyndon Evans and Philip Bryant. *LHC Machine*, volume 3. Journal of Instrumentation, aug 2008.
- [55] ALICE collaboration. *Alignment of the ALICE Inner Tracking System with cosmic-ray tracks*, volume 5. Journal of Instrumentation, Mar 2010.
- [56] R. Aaij, C. Abellán Beteta, T. Ackernley, B. Adeva, M. Adinolfi, H. Afsharnia, C.A. Aidala, S. Aiola, Z. Ajaltouni, S. Akar, and et al. Measurement of the electron reconstruction efficiency at lhcb. 14(11):P11023–P11023, Nov 2019.
- [57] S Chatrchyan, G Hmayakyan, V Khachatryan, and et al. The CMS experiment at the CERN LHC. The Compact Muon Solenoid experiment. *JINST*, 3:S08004. 361 p, 2008. Also published by CERN Geneva in 2010.
- [58] The ATLAS Collaboration, G Aad, E Abat, J Abdallah, A A Abdelalim, and et al. *The ATLAS Experiment at the CERN Large Hadron Collider*, volume 3. Journal of Instrumentation, aug 2008.